Conformational and functional changes of the native neuropeptide somatostatin occur in the presence of copper and amyloid-β

Jiyeon Han [1], Jiwon Yoon [2], Jeongcheol Shin [1], Eunju Nam [1], Tongrui Qian [3], Yulong Li [3,4,5], Kiyoung Park [1✉], Seung-Hee Lee [2✉] and Mi Hee Lim [1✉]

The progression of neurodegenerative disorders can lead to impaired neurotransmission; however, the role of pathogenic factors associated with these diseases and their impact on the structures and functions of neurotransmitters have not been clearly established. Here we report the discovery that conformational and functional changes of a native neuropeptide, somatostatin (SST), occur in the presence of copper ions, metal-free amyloid-β (Aβ) and metal-bound Aβ (metal–Aβ) found as pathological factors in the brains of patients with Alzheimer's disease. These pathological elements induce the self-assembly of SST and, consequently, prevent it from binding to the receptor. In the reverse direction, SST notably modifies the aggregation profiles of Aβ species in the presence of metal ions, attenuating their cytotoxicity and interactions with cell membranes. Our work demonstrates a loss of normal function of SST as a neurotransmitter and a gain of its modulative function against metal–Aβ under pathological conditions.

Neurotransmitters are essential for signal transduction throughout entire nervous systems[1–6]. Neuronal communications accompanied by a variety of neurotransmitters, including amino acids, small molecules, metal ions, and neuropeptides, maintain the balance between excitatory and inhibitory synaptic transmission[2–4]. Neuropeptides as one of the key neurotransmitters are released from the activated neurons and bind to receptors at cellular membranes of nearby neurons, subsequently initiating intracellular signalling pathways[1,4,5]. Given that dysfunction in neurotransmission is closely related to the pathologies of neurodegenerative disorders such as Alzheimer's disease (AD)[1,6–11], the activities of neuropeptides can be disrupted by pathogenic factors in diseased states.

In the AD-affected brain, senile plaques, primarily composed of amyloid-β (Aβ) aggregates and metal ions, are found[7,8,12]. Aβ as an intrinsically disordered peptide tends to form aggregates, including oligomers and fibrils[13], as shown in Fig. 1a, and soluble and structured oligomers have been shown to be toxic[11,13–15]. The accumulation of highly concentrated metal ions into senile plaques causes metal ion dyshomeostasis and miscompartmentation, lowering the efficiency of neurotransmission and the activities of metalloenzymes[10,12,16,17]. Metal ions such as Cu(II) and Zn(II) are coordinated to Aβ producing metal-bound Aβ (metal–Aβ; Fig. 1a) that can generate and stabilize toxic structured Aβ oligomers[18–22]. Furthermore, recent studies revealed the spatial overlap of senile plaques in the frontal cortex and hippocampus with somatostatin (SST; Fig. 1b), a neuropeptide that binds to SST receptors (SSTRs) at cellular membranes[23–25]. SST regulates the endocrine system and neurotransmission through G-protein-coupled receptor (GPCR)-mediated signalling pathways[23,26,27]. SST was also reported to interact with Aβ and metal ions, suggesting its link to the amyloid cascade and metal

ion hypotheses towards the pathology of AD[28–31]. Despite these observations, the conformational and functional changes of SST in the presence of pathological elements in the AD-affected brain remain unkown.

We questioned whether SST is structurally and functionally changed under pathological conditions associated with AD and if such variations can modify the aggregation and cytotoxicity profiles of Aβ. Thus, we determined the molecular-level interactions of SST with metal ions, metal-free Aβ and metal–Aβ and their influence on the conformational transition and GPCR binding of SST. Moreover, we evaluated the effects of SST on the aggregation and toxicity of metal-free and metal-bound Aβ species following its structural alteration. Overall, our studies validate a loss of normal function and a gain of modulative function of SST through direct contacts with pathological components found in AD, which illuminates distinct activities of the neuropeptide in the development of the disease.

Results and discussion

Conformational and functional changes of SST by metal ions.
The conformational alteration of SST in the presence of metal ions was investigated by tricine-containing polyacrylamide gel electrophoresis (tricine–PAGE) and circular dichroism (CD) spectroscopy. SST was incubated with or without metal ions for multiple incubation time points (Fig. 2a). The size distribution of the resultant SST species was first monitored by tricine–PAGE with Western blotting using an anti-SST antibody. As presented in Fig. 2b, a single band below 2 kDa corresponding to monomeric SST (1.6 kDa) was detected up to 24 h incubation under both metal-free and Zn(II)-present conditions. Thus, metal-free and Zn(II)-added SST did not undergo the aggregation, which is consistent with previously
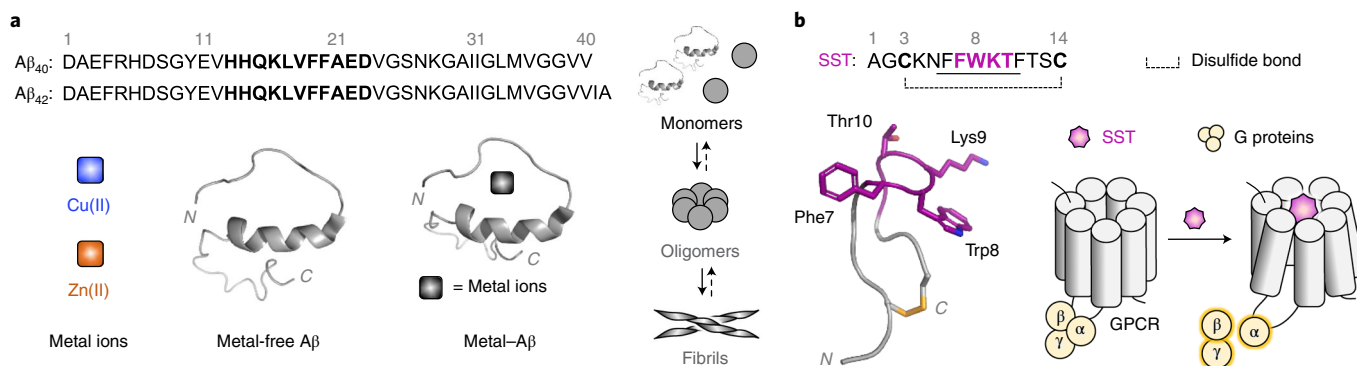
Fig. 1 | Pathogenic factors of AD and SST studied in this work. a, Metal ions, metal-free Aβ and metal–Aβ co-localized with SST in senile plaques. A partially folded Aβ40 (PDB 2LFM[46]) was presented as a representative structure in an aqueous environment. The amino acid residues in a 3₁₀ helix are in bold. Aβ tends to aggregate into oligomers and fibrils. Cu(II) and Zn(II) can generate and stabilize toxic Aβ oligomers. **b**, Structure of SST determined by NMR spectroscopy (PDB 2MI1[32]). The amino acid residues in a β-hairpin structure are underlined. The disulfide bond between Cys3 and Cys14 is indicated as a dashed line. The amino acid residues highlighted in magenta are critical for SST binding to GPCRs.

reported observations regarding SST[32,33]. Interestingly, the smearing in the gel was noticeably exhibited (<~15 kDa) upon treatment of SST with Cu(II) for 8 and 24 h, indicative of the oligomerization of SST induced by Cu(II).

The impact of metal ions on the secondary structure of SST was monitored by CD spectroscopy. As illustrated in Fig. 2c, our CD measurements demonstrated that the random coil conformation in SST was mainly observed with a local minimum at ~200 nm in both the absence and presence of metal ions at an early incubation time point (for example, 5 min). In addition, a broad minimum at ~235 nm appeared notably only in the sample of Cu(II)-added SST, which implies that Cu(II) binding of SST may contribute to the alignment of the disulfide bond between Cys3 and Cys14 in aqueous media[32,34,35]. After 24 h incubation, the random coil structure was maintained under metal-free and Zn(II)-present conditions. Interestingly, all the CD signals of SST were decreased upon treatment of Cu(II) with SST for 24 h, indicating that Cu(II) aggravates SST aggregation[32]. As displayed in Supplementary Fig. 3a, the addition of a hexadentate ligand, EDTA (ethylenediaminetetraacetic acid), did not recover the CD signals shown in Cu(II)-added SST. These observations imply the irreversible structural variation of SST incubated with Cu(II).

To identify whether metal ions affect the receptor-binding property of SST that initiates cellular signalling pathways[23,26,27], we employed the genetically encoded GPCR-activation-based sensor (GRAB_SST). GRAB_SST mimics the binding profiles of SST to its receptor type 5 (SSTR5), as illustrated in Fig. 2d[36]. The circularly permuted green fluorescent protein (cpEGFP) is inserted at the third intracellular loop in a scaffold of SSTR5 to enhance the fluorescence signal upon its conformational change mediated by SST binding. Note that the exogenously expressed GRAB_SST sensor recruits negligible downstream signalling molecules[36]; thus, it only detects SST binding to SSTR5, indicating a change in fluorescence without any physiological variations through intracellular signalling cascades. The effective concentration (EC_50) value of the GRAB_SST sensor against SST was measured to be $0.74 \pm 0.02\,\mu M$ under our experimental settings, as shown in Extended Data Fig. 1a, which is in a reliable range according to previously reported studies[36–38]. Moving forwards, we treated SST incubated with or without metal ions to HEK293T cells expressing the GRAB_SST sensor. As summarized in Fig. 2e and Extended Data Fig. 1b,c, the receptor binding of SST was inhibited by ~22% by incubation with Cu(II) compared with that of metal-free SST. In the case of Zn(II), the ability of SST to bind to SSTR5 was maintained. The control samples without SST did not exhibit notable fluorescence changes upon treatment onto the cells (Fig. 2e).

Given that the Phe7, Trp8, Lys9, and Thr10 residues in the β-hairpin are essential for the interaction between SST and SSTR[23,39], the microenvironment of this motif was further probed by measuring the Trp fluorescence of SST with and without metal ions. As indicated in Fig. 2f, the maximum fluorescence (F_max) of metal-free SST was lowered by ~25% after 24 h incubation. In the presence of Cu(II), the F_max value was reduced even at 5 min incubation, exhibiting an additional decrease in fluorescence by ~75% at 24 h incubation. Furthermore, Cu(II)-treated SST presented a slight blue shift of the maximum wavelength (λ_max) by ~5 nm upon incubation from 5 min to 24 h, indicating the increase in hydrophobicity around the motif responsible for GPCR binding[40]. Notably, the changes in the F_max and λ_max values of Cu(II)-treated SST were not restored by the addition of EDTA (Supplementary Fig. 3b). These observations suggest that Cu(II) may change the conformation of SST in an irreversible manner, possibly due to its aggregation upon binding to Cu(II). As expected from the studies using the GRAB_SST sensor, Zn(II) did not alter the fluorescence of SST. Collectively, Cu(II) can induce the aggregation of SST and interfere with its receptor binding. These results substantiate a loss of normal function of SST towards GPCR-driven signalling pathways.

Metal binding of SST. Given that the conformation and function of SST are altered in the presence of Cu(II), we probed its coordination to SST. The dissociation constant (K_d) of Cu(II)(SST) was first determined by fluorescence-quenching experiments[41]. The paramagnetic Cu(II) can quench the emission of a fluorophore (for example, Trp8) through photoinduced electron transfer[41,42]. As depicted in Supplementary Fig. 2a,b, the intrinsic fluorescence of SST was decreased by titrating various concentrations of CuCl₂ and Cu(NO₃)₂. The K_d value for Cu(II)(SST) was determined to be in a micromolar range.

Electronic absorption (Abs) and electron paramagnetic resonance (EPR) spectroscopies were employed to probe the Cu(II)-binding properties of SST under the same conditions used to obtain the K_d value of Cu(II)(SST). As illustrated in Fig. 3a, in the absence of SST, aqueous cupric ions displayed minor Abs intensities in the visible region, as their d–d transitions are strictly forbidden due to their centrosymmetric nature. Upon treatment with 1 equiv. of SST, however, a new Abs band appeared at ~590 nm (17,000 cm⁻¹), indicative of Cu(II) coordination to SST. The addition of EDTA to the solution containing Cu(II) and SST down-shifted the Abs band to ~720 nm (14,000 cm⁻¹). These alterations in ligand field were also observed in EPR spectra, as presented in Fig. 3b. Compared to the aqueous Cu(II) solution, the Cu(II)-incubated SST solution
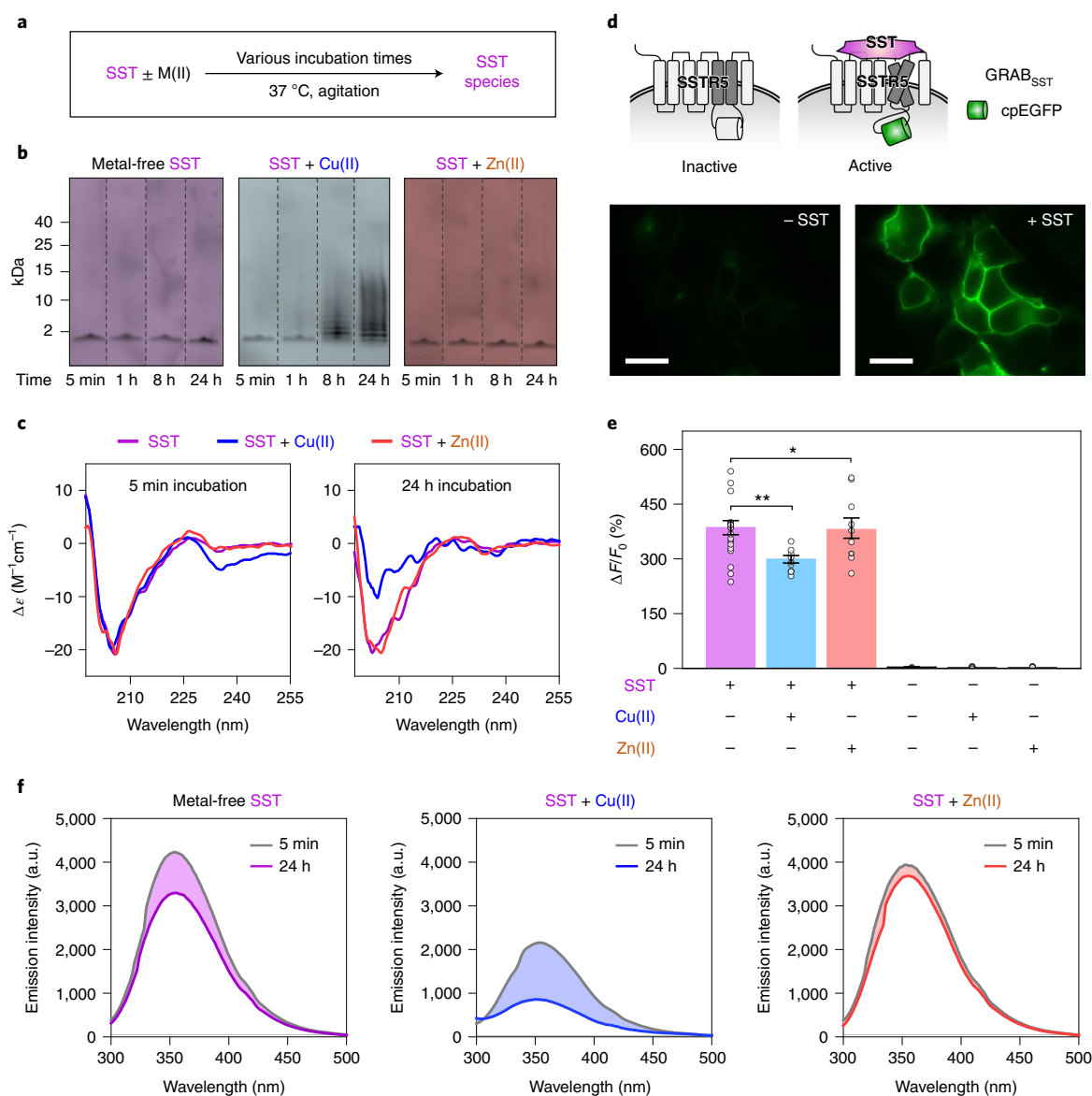
Fig. 2 | Conformational and functional changes of SST upon incubation with metal ions. a, Scheme of the experiments. **b**, Size distribution of the resultant SST species with or without metal ions probed by tricine–PAGE with Western blotting using an anti-SST antibody. Conditions: $[SST] = 100\,\mu M$; $[MCl_2] = 100\,\mu M$; 20 mM HEPES, pH 7.4, 150 mM NaCl; 37 °C; constant agitation (250 r.p.m.). All measurements were performed in triplicate. **c**, Change in the secondary structure of SST in the absence and presence of metal ions monitored by CD spectroscopy. Conditions: $[SST] = 100\,\mu M$; $[M(NO_3)_2] = 100\,\mu M$; 20 mM HEPES, pH 7.4, 150 mM NaF; 37 °C; constant agitation (250 r.p.m.). Metal coordination depending on anions is negligible under our experimental conditions (Supplementary Figs. 1 and 2). **d**, Schematic descriptions of the GRAB$_{SST}$ sensor and live-cell imaging experiments. The GRAB$_{SST}$ sensor developed based on human SSTR5 was used. Scale bars, 20 μm. **e**, Binding of SST species produced upon 24 h treatment with and without metal ions to SSTR5 monitored by confocal microscopy. $\Delta F/F_0$ values were quantitatively analysed 3 min after addition of the samples. Data are presented as mean ± s.e.m.; $n = 4$–20 cells; the precise n can be found in Extended Data Fig. 1. P values are derived from a two-sided unpaired Kruskal–Wallis test with Bonferroni correction in comparison to the cells treated with metal-free SST: $P = 0.009$ for cells treated with SST and Cu(II); $P = 0.045$ for cells treated with SST and Zn(II). *$P < 0.05$, **$P < 0.01$. Conditions: $[SST] = 0.5\,\mu M$; $[MCl_2] = 0.5\,\mu M$; HEK293T cells. **f**, Change in the intrinsic Trp8 fluorescence upon incubation of metal-free and metal-added SST species. Conditions: $[SST] = 100\,\mu M$; $[MCl_2] = 100\,\mu M$; 20 mM HEPES, pH 7.4, 150 mM NaCl; 37 °C; constant agitation (250 r.p.m.); $\lambda_{ex} = 280$ nm; $\lambda_{em} = 300$–500 nm. The measurements were performed in triplicate.

displayed distinctive g_z and A_z hyperfine features at 2,600–3,200 G (Fig. 3b and Supplementary Fig. 4). Notably, while the aqueous Cu(II) solution featured two different species with g_zs of 2.262 and 2.295, the Cu(II)-incubated SST solution exhibited a more homogeneous Cu(II) hyperfine splitting pattern with a more reduced g_z value of 2.233, indicative of a rather specific binding site. Upon introduction of EDTA to the Cu(II)-incubated SST solution, two g_z features grew at 2.289 and 2.330 that match the previously reported

EPR signals of $[Cu(EDTA)]^{2-}$ and $[Cu(HEDTA)]^-$, respectively[43]. The reduced g_z value and up-shifted Abs band of the SST-bound Cu(II) species relative to those of the (H)EDTA-bound Cu(II) complexes reveal that SST provides stronger σ donation to the Cu(II) centre than the EDTA ligand as an elevated energy level of the Cu(II) $3d_{x^2-y^2}$-based molecular orbital can decrease the EPR g_z value and increase the d–d transition energies. These spectral data were utilized to search for the SST-bound Cu(II) structure.
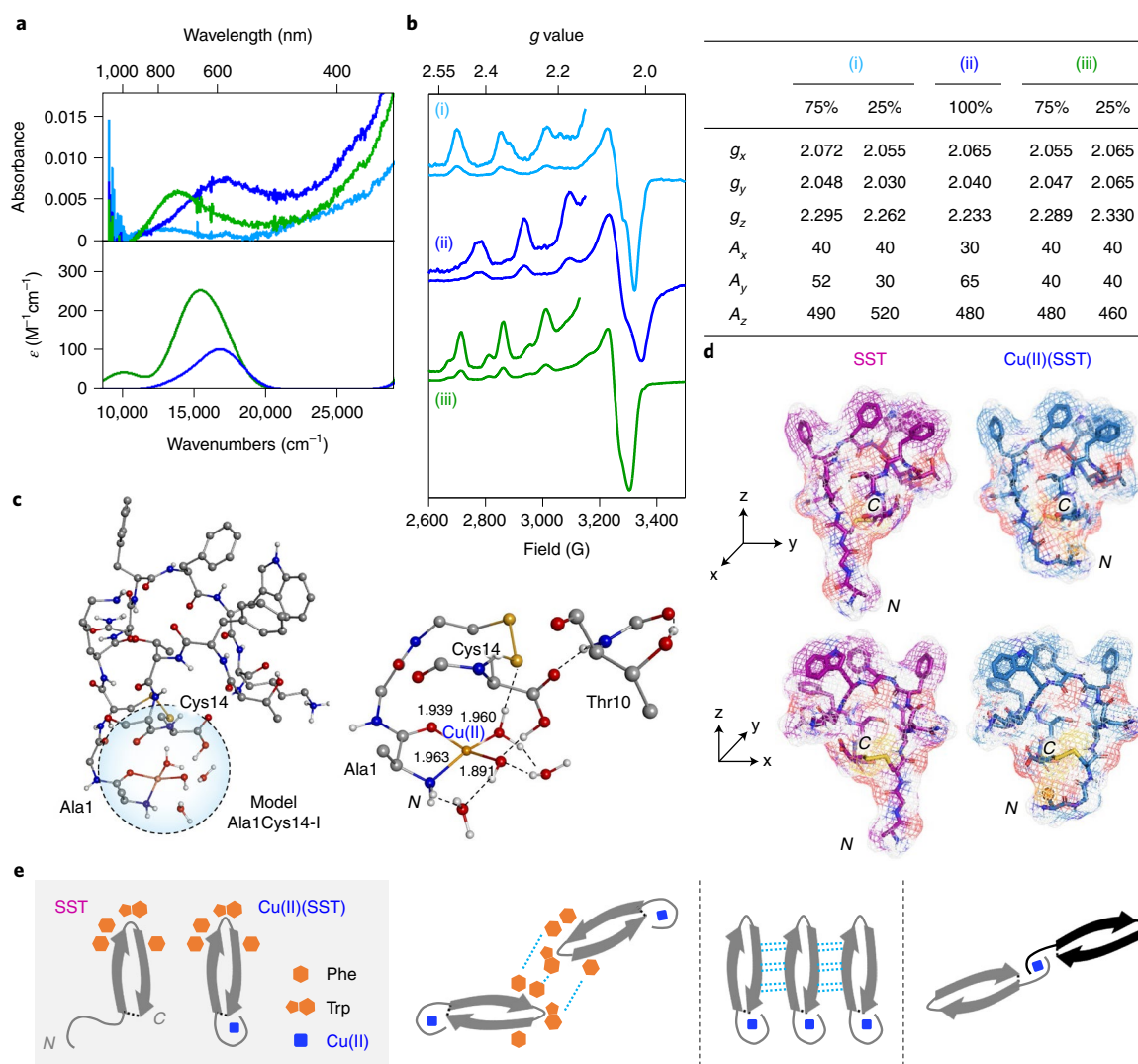
Fig. 3 | Cu(II) coordination to SST and proposed mechanisms for the nucleation of Cu(II)(SST). a, Top: Abs spectra of Cu(II) with or without SST followed by addition of EDTA. (i) CuCl$_2$ (aq.) (light blue); (ii) CuCl$_2$ (aq.) treated with SST (dark blue); (iii) CuCl$_2$ (aq.) incubated with SST, subsequently mixed with EDTA (green). Bottom: TDDFT-simulated Abs spectra of [Cu(HEDTA)]$^-$ and the Cu(II)(SST) model (**Ala1Cys14-I**) highlighted in green and blue, respectively. Conditions: [CuCl$_2$] = 100 μM; [SST] = 100 μM; [EDTA] = 100 μM; 20 mM HEPES, pH 7.4. **b**, EPR-monitored Cu(II) coordination to SST. The g and A_{Cu} (in MHz) values obtained from the samples (i)–(iii) are presented in the table. The A_z hyperfine features are magnified by four times for clarity. The simulations of these spectra are presented in Supplementary Fig. 4, showing that solutions (i) and (iii) contained two different species in a ratio of 3:1. The DFT-calculated EPR parameters for [Cu(HEDTA)]$^-$ and **Ala1Cys14-I** are described in Supplementary Table 1. Conditions: [CuCl$_2$] = 100 μM; [SST] = 100 μM; [EDTA] = 100 μM; 20 mM HEPES, pH 7.4; 100 K. **c**, A representative DFT model of Cu(II)(SST), **Ala1Cys14-I**. The truncated Cu(II) coordination sphere is given on the right. Three other different models with variations in hydrogen bonding are shown, with their relative potential energies, in Extended Data Fig. 2c. Orange, yellow, grey, blue, red, and white balls indicate copper, sulfur, carbon, nitrogen, oxygen and hydrogen atoms, respectively. Hydrogen atoms bonded to carbon atoms are omitted for clarity. **d**, Comparison between the DFT-optimized structures of metal-free SST and Cu(II)(SST). **e**, Proposed mechanisms for how the aggregation of SST upon binding to Cu(II) can be initiated. Left to right: hydrophobic interactions, antiparallel β-sheet formation and the complexation of Cu(II)(SST) with an additional SST.

To determine the Cu(II)(SST) structure that can reproduce the Abs and EPR spectral data, DFT models were constructed by introducing Cu(II) to plausible coordination sites, including the *N*-terminal primary amine (Ala1), the ε-amino group of Lys4 and Lys9, and the *C*-terminal carboxylate group (Cys14). Total 11 structures were geometry-optimized with their relative potential energies spanning from 0 to 34 kcal mol^{-1} (Extended Data Fig. 2 and Supplementary Figs. 5–7). These DFT models illustrate that the binding of two amino acid residues, such as the combinations of Ala1/Lys4, Ala1/Cys14 and Lys9/Cys14, can greatly modify the conformation of SST, while the coordination of Cu(II) to either Ala1 or Cys14 alone barely affects its configuration. Although the

Ala1/Lys4 coordination costs excessive energy, the Ala1/Cys14 or Lys9/Cys14 binding appears to be accessible given the DFT energy error of ~5 kcal mol^{-1} (Supplementary Table 1). To distinguish the structural candidates, their Abs spectra and EPR parameters were predicted on the Cu(II) sites, which were prepared by truncating the structures due to computational costs. To validate DFT methods, structurally better-established [Cu(EDTA)]$^{2-}$ and [Cu(HEDTA)]$^-$ complexes were used[43] (Supplementary Fig. 8). Our TDDFT computations tend to overestimate the energies of the Abs bands associated with *d*–*d* transitions, and EPR calculations underestimate the g_z values and their differences (Supplementary Fig. 9). Among the 11 models, only **Ala1Cys14-1** reproduces the decreases in the Abs

wavelength and the EPR g_z value, compared to the (H)EDTA-bound Cu(II) models, suggesting that Cu(II) can bind to the *N*-terminal primary amine, the backbone carbonyl group from Ala1, and water molecules that are hydrogen bonded to Cys14, as depicted in Fig. 3c. The ligated water molecule can form a strong hydrogen bond to the *C*-terminal carboxylate group and become deprotonated. Notably, this Cu(II) coordination to SST folds its *N*-terminus and, consequently, produces a compact structure, relative to that of Cu(II)-free SST, as shown in Fig. 3d and Supplementary Fig. 10.

Following the conformational change of SST upon binding to Cu(II), potential mechanisms for the aggregation of Cu(II)(SST) at the early stage are proposed (Fig. 3e): (1) hydrophobic interactions, (2) antiparallel β-sheet formation and (3) the complexation of Cu(II)(SST) with an additional SST. First, Cu(II) coordination to SST results in its compact and more folded conformation; thus, it could increase the probability of hydrophobic interactions between SST monomers. The aromatic amino acid residues in SST (that is, Phe6, Phe7, Trp8 and Phe11) could be involved in hydrophobic interactions, including π–π or C–H–π interactions. As the second mechanism, Cu(II)(SST) could form β-sheets through intermolecular interactions. Cu(II) binding to SST could trigger its *N*-terminal folding, affording a compact structure to overcome the critical assembly concentration[44] under our experimental conditions. Lastly, Cu(II)(SST) could recruit an additional SST to produce Cu(II)(SST)$_2$. Based on the DFT model, the Cu(II)-binding site is exposed to the solvent and, thus, an additional SST can be accessible to the Cu(II) centre. Note that copper–O$_2$ chemistry may not be involved in the aggregation of SST (Supplementary Fig. 11).

In the case of Zn(II)(SST) exhibiting limited spectral changes, compared to Zn(II)-free SST, its K_d value was estimated by competitive binding studies employing Zincon (2-carboxy-2′-hydroxy-5′-sulfoformazyl-benzene monosodium salt), which is a colorimetric metal chelator with 1:1 Zn(II)-to-ligand stoichiometry[45]. As shown in Supplementary Fig. 2c,d, upon titration of SST into Zn(II)(Zincon), the absorbance at 618 nm was reduced, supporting the complexation of Zn(II) with SST over Zincon. A micromolar K_d value for Zn(II)(SST) was measured using ZnCl$_2$ and Zn(NO$_3$)$_2$.

Effects of Aβ on the aggregation and receptor binding of SST. To verify the effects of Aβ on the conformation and function of SST, we first analysed the samples of SST (1,638 Da) incubated with Aβ$_{40}$ (4,328 Da) or Aβ$_{42}$ (4,515 Da) in the absence and presence of metal ions by electrospray ionization–mass spectrometry (ESI–MS) (Fig. 4a,b and Supplementary Figs. 12 and 13). As displayed in Fig. 4b, in the presence of Cu(II), new peaks appeared at 1,194 *m/z* and 1,206 *m/z* that originate from +5-charged species, in addition to 820 *m/z* and 1,443 *m/z* corresponding to monomeric SST^{2+} and Aβ$_{40}$$^{3+}$, respectively. Under Zn(II)-present and metal-free conditions, the +5-charged peak at 1,194 *m/z* was detected. To assign the aforementioned ions, we carried out tandem MS (ESI–MS^2) by applying the collision-induced dissociation (CID) energy against the peak of interest, as presented in Fig. 4b and Supplementary Fig. 13. Our tandem MS studies revealed that the peak at 1,194 *m/z* is composed of +2-charged SST and +3-charged Aβ, thus representing the formation of a heterodimer. More interestingly, the CID-associated fragmentation of the peak at 1,206 *m/z* indicated multiply charged SST and Aβ$_{40}$, both of which are bound to Cu(II). This implies the generation of a ternary complex comprised of SST, Cu(II) and Aβ$_{40}$. In the case of Aβ$_{42}$, the interactions of SST towards metal-free and metal-added Aβ$_{42}$ were similar to those observed from Aβ$_{40}$ with and without metal ions (Supplementary Fig. 12).

To visualize the potential interactions between SST and Aβ, we performed docking studies employing their structures that were obtained by NMR spectroscopy in an aqueous solution (for SST, PDB 2MI1[32]; for Aβ$_{40}$, PDB 2LFM[46]). As illustrated in Fig. 4c, when

SST was bound to Aβ$_{40}$, multiple intermolecular interactions were indicated ($\Delta G = -11.6$ kcal mol^{-1}). Hydrogen bonds between SST and Aβ$_{40}$ were indicated: (i, ii) the backbone carbonyl group of Cys3 in SST and the backbone amide moiety of His6 or Asp7 in Aβ$_{40}$; (iii) the backbone amide group of Asn5 in SST and the side chain of Ser8 in Aβ$_{40}$; (iv) the side chain amide moiety of Asn5 in SST and the backbone carbonyl group of Ser8 in Aβ$_{40}$. In addition, π–π stacking of Phe6 in SST and Tyr10 in Aβ$_{40}$ was observed. Note that other conformers with the ΔG values lower than -11.0 kcal mol^{-1} were also analysed and are summarized in Supplementary Fig. 14.

We further probed the impact of metal–Aβ and metal-free Aβ on the aggregation of SST by tricine–PAGE with Western blotting using an anti-SST antibody. As depicted in Fig. 4d, the sample of SST presented the enhanced smearing larger than 10 kDa in the gel by incubation with Cu(II)–Aβ$_{40}$ for 8 and 24 h. Thus, Cu(II)–Aβ$_{40}$ could induce the production of SST oligomers. In the case of Zn(II)–Aβ$_{40}$ and metal-free Aβ$_{40}$, SST aggregates in a range from 5 to 15 kDa were formed after 8 and 24 h treatment. To evaluate the stability of the resultant SST aggregates, we additionally conducted sodium dodecyl sulfate (SDS)–PAGE of the samples pretreated with urea. The size of the SST aggregates produced with Cu(II)–Aβ$_{40}$ and Zn(II)–Aβ$_{40}$ was mainly between 10 and 15 kDa, and these aggregates were relatively resistant to SDS. Distinctly, in the case of SST aggregates formed with metal-free Aβ$_{40}$, the smearing larger than 5 kDa was weakened with a relatively prominent band below 2 kDa, which presents the different stability of SST oligomers under metal-absent conditions. In a similar trend to Aβ$_{40}$, SST was observed to aggregate in the presence of metal–Aβ$_{42}$ and metal-free Aβ$_{42}$, as illustrated in Supplementary Fig. 15. The SST aggregates showed smearing bands larger than ~10 kDa in SDS–PAGE, indicating relatively stable oligomers against SDS. Together, metal–Aβ and metal-free Aβ can trigger the aggregation of SST to different degrees. Previous studies described that glycosaminoglycan heparin containing sulfate groups could accelerate the self-assembly of SST (pI ≈ 8.6) by hindering the electrostatic repulsion between SST monomers[32,33]. Considering the pI value of Aβ (~5.5)[20], electrostatic interactions of SST with metal–Aβ and metal-free Aβ may induce the aggregation of SST as heparin does.

Finally, we verified the ability of the SST aggregates generated with Aβ species to bind to the receptor through live-cell imaging employing the GRAB$_{SST}$ sensor. We incubated SST with Aβ$_{40}$ in the absence and presence of metal ions for 24 h followed by addition to HEK293T cells expressing the GRAB$_{SST}$ sensor. As shown in Fig. 4e and Extended Data Fig. 3, SST treated with metal–Aβ$_{40}$ or metal-free Aβ$_{40}$ could not bind to the receptor by 40–55%, relative to SST only. Note that Aβ$_{40}$ with and without metal ions did not affect the fluorescence of the GRAB$_{SST}$ sensor, consistent with the previous study reporting no uptake of Aβ species into HEK293T cells[47]. This observation can exclude the possibility of Aβ to sterically block the SST-binding site in SSTR5. Collectively, our studies demonstrate that both metal–Aβ and metal-free Aβ provoke the aggregation of SST to different extents and disrupt its SSTR binding.

Impact of SST on Aβ aggregation. We examined the influence of SST on the aggregation of metal–Aβ and metal-free Aβ, as described in Fig. 5 and Supplementary Figs. 16 and 17. The aggregation kinetics of Aβ was traced with and without metal ions by the thioflavin-T (ThT) assay, which is used for quantifying the amount of β-sheet-rich peptide species[48]. As displayed in Fig. 5b, in the absence of SST, Cu(II)–Aβ$_{42}$ and Zn(II)–Aβ$_{42}$ reached the plateau at 1 and 4 h, respectively. In particular, the fluorescence intensity of Cu(II)–Aβ$_{42}$ was decreased by ~20% after the plateau possibly because of the precipitation or the formation of ThT-unreactive species. Upon incubation of 1 equiv. of SST with metal–Aβ$_{42}$, the ThT fluorescence was indicated to be greater than that of metal–Aβ$_{42}$ without SST. Furthermore, the aggregation kinetics of metal–Aβ$_{42}$
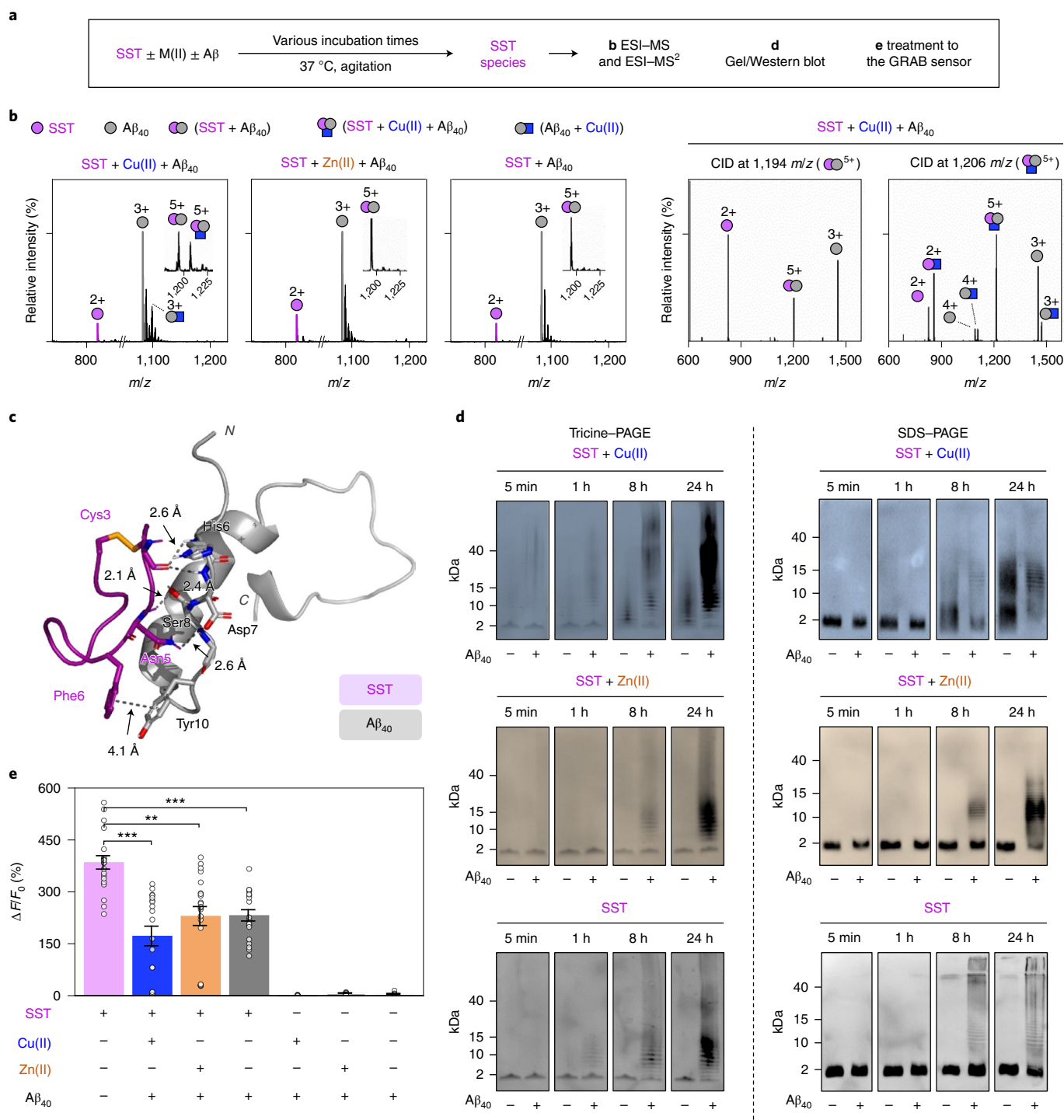
Fig. 4 | Aβ-mediated aggregation of SST in the absence and presence of metal ions. a, Scheme of the experiments. **b**, SST binding to Aβ$_{40}$ with and without metal ions monitored by ESI–MS and ESI–MS^2. SST and Aβ$_{40}$ are represented by purple and grey circles, respectively. Cu(II) is indicated as a blue rectangle. The peaks corresponding to [SST + Aβ$_{40}$]$^{5+}$ and [SST + Cu(II) + Aβ$_{40}$]$^{5+}$, found in the sample containing SST, Cu(II) and Aβ$_{40}$, were further characterized by ESI–MS^2. Charge states are marked above the peaks in the MS spectra. Conditions: [SST] = 100 μM; [MCl$_2$] = 100 μM; [Aβ$_{40}$] = 100 μM; 20 mM ammonium acetate; 37 °C; 3 h incubation; constant agitation (250 r.p.m.). The measurements were conducted in triplicate. The samples were diluted 10-fold before injection into the mass spectrometer. **c**, Possible interactions between SST (PDB 2MI1[32]) with Aβ$_{40}$ (PDB 2LFM[46]) visualized by docking studies. SST and Aβ$_{40}$ are depicted in purple and grey, respectively. The dashed lines indicate possible hydrogen bonds (within 3.0 Å) and π–π interactions (within 4.5 Å) between the two peptides. **d**, Size distribution of the resultant SST species with and without Aβ probed by gel/Western blot with an anti-SST antibody. Conditions: [SST] = 100 μM; [MCl$_2$] = 100 μM; [Aβ$_{40}$] = 100 μM; 20 mM HEPES, pH 7.4, 150 mM NaCl; 37 °C; constant agitation (250 r.p.m.). The measurements were performed in triplicate. **e**, Receptor binding of SST species incubated with Aβ measured by confocal microscopy. Data are presented as mean ± s.e.m.; n = 19–21 cells; the precise n can be found in Extended Data Fig. 3. P values are derived from a two-sided unpaired Kruskal–Wallis test with Bonferroni correction in comparison to the cells treated with metal-free SST: P = 2.0 × 10^{-6} for cells treated with SST, Cu(II) and Aβ; P = 0.001 for cells treated with SST, Zn(II) and Aβ; P = 1.4 × 10^{-4} for cells treated with SST and Aβ. **P < 0.01, ***P < 0.001. Conditions: [Aβ$_{40}$] = 0.5 μM; [MCl$_2$] = 0.5 μM; [SST] = 0.5 μM; HEK293T cells.
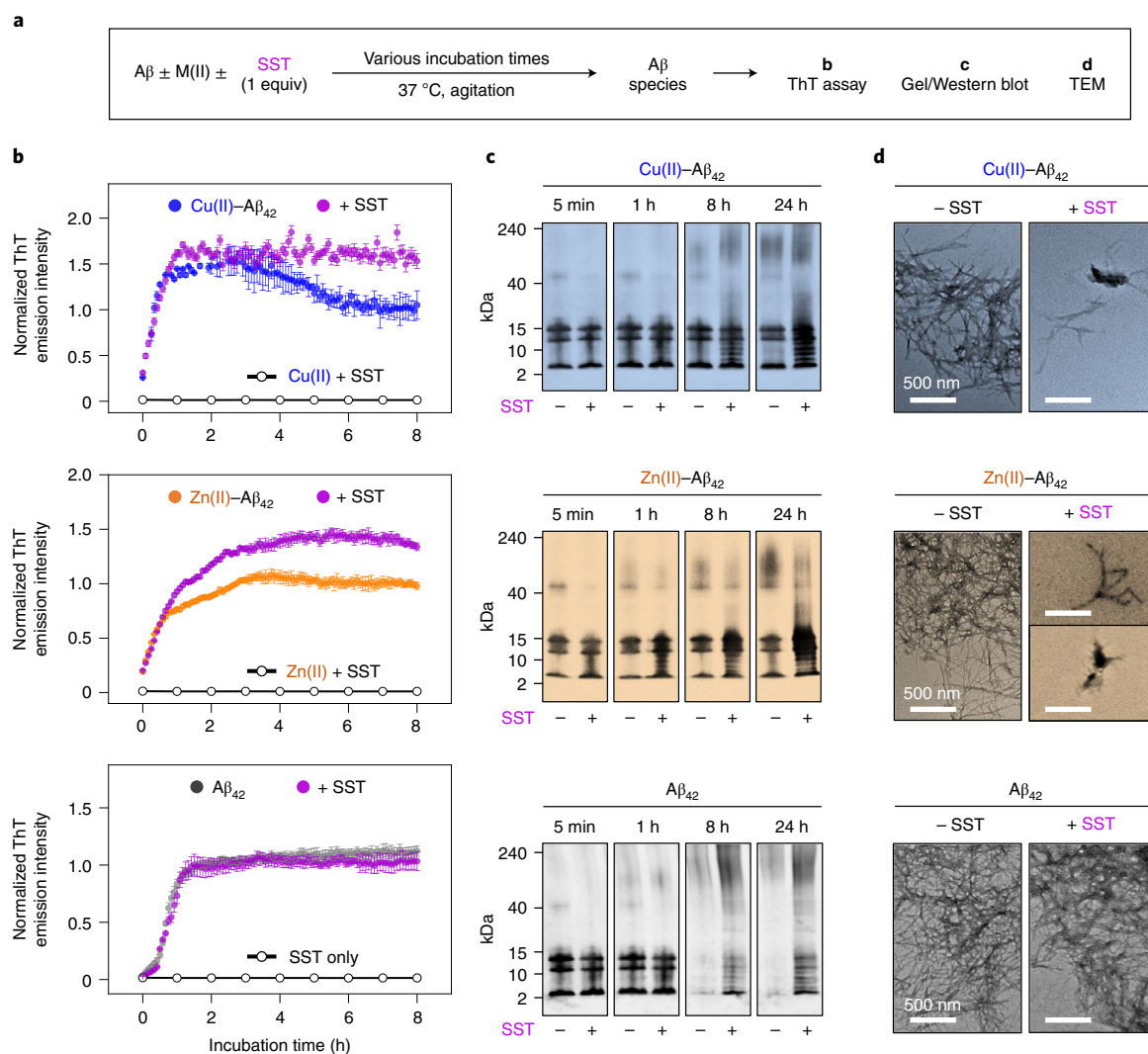
Fig. 5 | Effects of SST on Aβ aggregation with and without metal ions. a, Scheme of the aggregation studies. **b**, Aggregation kinetics of metal–Aβ$_{42}$ and metal-free Aβ$_{42}$ species upon treatment of SST analysed by the ThT assay. Conditions: [Aβ$_{42}$] = 20 μM; [CuCl$_2$] = 18 μM; [ZnCl$_2$] = 20 μM; [SST] = 20 μM; [ThT] = 20 μM; 20 mM HEPES, pH 7.4, 150 mM NaCl; 37 °C; constant agitation (250 r.p.m.); λ$_{ex}$ = 440 nm; λ$_{em}$ = 490 nm. The error bars denote mean ± s.e.m. for n = 6 examined over three independent experiments. **c**, Size distributions of the resultant metal–Aβ$_{42}$ and metal-free Aβ$_{42}$ species monitored by tricine–PAGE with Western blotting using an anti-Aβ antibody (6E10). Conditions: [Aβ$_{42}$] = 100 μM; [MCl$_2$] = 100 μM; [SST] = 100 μM; 20 mM HEPES, pH 7.4, 150 mM NaCl; 37 °C; constant agitation (250 r.p.m.). **d**, Morphologies of the resultant peptide aggregates detected by TEM. Conditions: [Aβ$_{42}$] = 100 μM; [MCl$_2$] = 100 μM; [SST] = 100 μM; 20 mM HEPES, pH 7.4, 150 mM NaCl; 37 °C; constant agitation (250 r.p.m.). Scale bars, 500 nm. All measurements were performed in triplicate.

was identified in the presence of sub- and supra-equimolar concentrations of SST, as presented in Supplementary Fig. 16a. The ThT emission intensity of metal–Aβ$_{42}$ with SST was increased in a concentration-dependent manner, manifesting the effect of SST on the generation of β-sheet-rich metal–Aβ$_{42}$ aggregates. For metal-free Aβ$_{42}$, the fluorescence was slightly changed even with 5 equiv. of SST compared with that incubated with 0.5 and 1 equiv. of SST. As shown in Supplementary Fig. 16b, the $t_{1/2}$ values for the aggregation of metal–Aβ$_{42}$ and metal-free Aβ$_{42}$ were analysed, where $t_{1/2}$ is the half-time when the fluorescence intensity reaches 50% of its maximum value. Based on the calculated $t_{1/2}$ values, the overall aggregation kinetics of metal–Aβ$_{42}$ was delayed by SST. Note that SST could not significantly affect the aggregation kinetics of metal-free Aβ$_{42}$. This observation is distinct from previously reported studies exhibiting the inhibition of metal-free Aβ$_{42}$ by SST[29,30], which possibly results from different experimental conditions (for example, concentrations of Aβ and SST, pH, ionic strength and the presence

of organic solvents). In the case of Cu(II)–Aβ$_{40}$ and Zn(II)–Aβ$_{40}$, SST could reduce the amount of the ThT-reactive species through the elongation phase and the plateau, respectively, as described in Supplementary Fig. 17b. The influence of SST on the aggregation of metal–Aβ$_{40}$ was also dependent on its stoichiometry to metal–Aβ$_{40}$ (Supplementary Fig. 16c). No notable fluorescence was observed from the samples containing SST with or without metal ions under our experimental conditions. Therefore, SST can vary the aggregation kinetics of Aβ species, more noticeably in the presence of metal ions.

Next, the molecular weight distribution of Aβ species (4–240 kDa) upon incubation with SST was determined by tricine–PAGE with Western blotting using an anti-Aβ antibody (6E10) that can detect the N-terminal region of Aβ[49]. As shown in Fig. 5c, Aβ$_{42}$ oligomers below 15 kDa, including trimers and tetramers, were observed in the absence of SST at early incubation time points under metal-present conditions. In contrast, the amount of
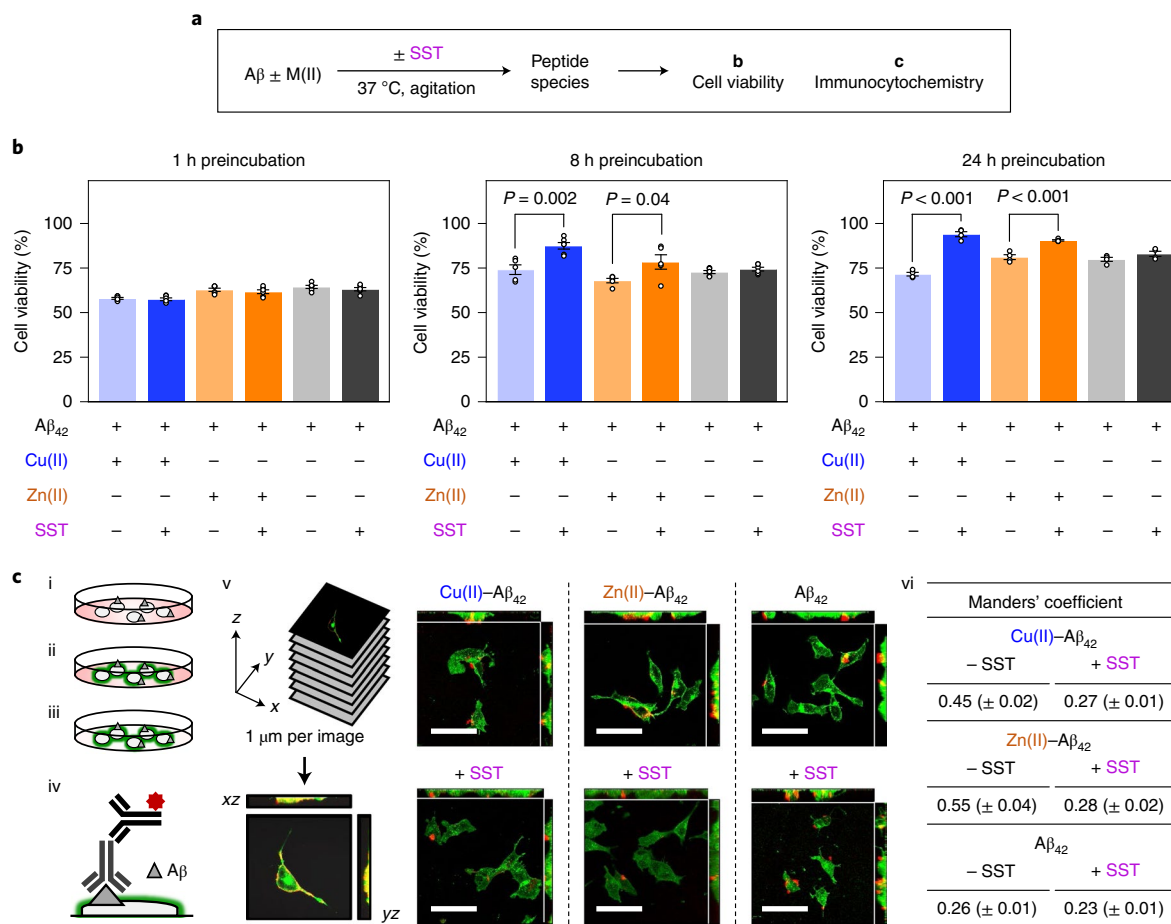
Fig. 6 | Influence of SST on the cytotoxicity induced by Aβ species in the absence and presence of metal ions. a, Scheme of the cell studies. **b**, Survival of the cells treated with Aβ$_{42}$ and SST with or without metal ions incubated for 1, 8 and 24 h. Cell viability, determined by MTT assay, was calculated in comparison to that with an equivalent amount of the buffered solution (20 mM HEPES, pH 7.4, 150 mM NaCl). Conditions: [Aβ$_{42}$] = 10 μM; [MCl$_2$] = 10 μM; [SST] = 10 μM; SH-SY5Y cells that were non-differentiated. The error bars denote mean ± s.e.m. for $n = 6$ examined over three independent experiments. P values are derived from a two-sided unpaired Student's t-test in comparison to the cells untreated with SST. **c**, Live-cell localization of Aβ$_{42}$ incubated with SST. (i) Treatment of the samples with cells for 24 h; (ii) membrane staining for 30 min ($\lambda_{ex} = 488$ nm; $\lambda_{em} = 501$ nm); (iii) cell fixation; (iv) labelling Aβ species by an anti-Aβ primary antibody (6E10) and a goat anti-mouse secondary antibody conjugated with the Alexa 647 fluorophore ($\lambda_{ex} = 652$ nm; $\lambda_{em} = 668$ nm); (v) three-dimensional (3D) imaging by z-stacking. (vi) Manders' coefficients were calculated for the 3D analysis of the co-localization of two fluorophores in the cells. The bright-field images are presented in Supplementary Fig. 21. Conditions: [Aβ$_{42}$] = 10 μM; [MCl$_2$] = 10 μM; [SST] = 10 μM; SH-SY5Y cells that were non-differentiated. Scale bars, 50 μm. Data are presented as mean ± s.e.m. of three independent experiments ($n = 3$).

such oligomeric species was reduced after 8 h incubation without SST and metal ions. Upon treatment of SST with metal–Aβ$_{42}$ and metal-free Aβ$_{42}$ for 8 and 24 h, the smearing in the gels between 4 and 15 kDa was monitored, indicative of the formation of multiple oligomers composed of either Aβ$_{42}$, SST or both, with and without metal ions. These observations regarding the intermolecular interactions between SST and Aβ$_{42}$ oligomers in the absence and presence of metal ions were supported by the ESI–MS studies, as depicted in Supplementary Fig. 18. The morphology of the resultant large-sized peptide aggregates (>240 kDa) was detected by transmission electron microscopy (TEM). As displayed in Fig. 5d, the morphology of the Aβ$_{42}$ aggregates produced with metal ions and SST was indicated to be a mixture of shorter fibrils and amorphous aggregates, compared to branched fibrils shown in SST-free metal–Aβ$_{42}$ aggregates. No morphological change of metal-free Aβ$_{42}$ incubated with SST was indicated, relative to that without SST, exhibiting large and branched fibrils. The effect of SST on the molecular weight distribution of metal–Aβ$_{40}$ upon aggregation was less noticeable, but smaller fibrils of metal–Aβ$_{40}$ were produced in the presence of SST,

probed by tricine–PAGE with Western blotting and TEM, respectively (Supplementary Fig. 17c,d). Compared to metal–Aβ$_{40}$, the smearing band of metal-free Aβ$_{40}$ vanished with treatment of SST, showing amorphous Aβ$_{40}$ aggregates that were monitored by TEM.

Moreover, the effect of SST on the aggregation of Aβ species under metal-present conditions was further analysed. As shown in Supplementary Fig. 19a, SST was preincubated with Cu(II) or Zn(II) for 1, 8, and 24 h and then treated with metal-free Aβ$_{42}$. Metal-treated SST could noticeably reduce the amount of the ThT-reactive species of Aβ$_{42}$, indicative of forming amorphous aggregates (Supplementary Fig. 19b). This observation is similar to that from the aggregation kinetics of metal-added Aβ$_{42}$, which suggests that metal ions bound to SST could be sequestrated by Aβ, as expected from their metal-binding affinities (K_ds for Cu(II)(Aβ) and Zn(II)(Aβ), 10^{-10} M and 10^{-6} M, respectively[8]; K_ds for Cu(II)(SST) and Zn(II)(SST), ~10^{-5} M; Supplementary Fig. 2). The size distribution of the resultant Aβ species was also monitored by tricine–PAGE with Western blotting (6E10) (Supplementary Fig. 19c). When SST was preincubated with metal ions for 1, 8, and 24 h and

then treated with $A\beta_{42}$ for an additional 24 h, various-sized $A\beta$ species were produced with an increase in the formation of oligomers of ~15 kDa, which was also observed from the sample of metal–$A\beta_{42}$ incubated with SST, relative to SST-free metal–$A\beta_{42}$. Such effects were more notable as preincubation time increased. Therefore, metal ions bound to SST could be chelated out by $A\beta$ and the resultant SST species subsequently affect the aggregation of metal–$A\beta$ species. Taken together, the aggregation of both $A\beta_{42}$ and $A\beta_{40}$ can be altered by treatment of SST, to different degrees, noticeably in the presence of metal ions. The different reactivity of SST with metal–$A\beta_{42}$ over metal–$A\beta_{40}$ may result from their distinct aggregation properties generating different conformational distributions of $A\beta$ aggregates (particularly, oligomers) upon aggregation[50,51].

Cytotoxicity of metal–$A\beta$ and metal-free $A\beta$ treated with SST.
$A\beta$ species can interact with cell membranes and, consequently, cause cytotoxicity through multiple pathways such as blocking cellular receptors and forming ion channels[11,13–15,52]. Thus, we investigated the effects of SST on the cytotoxicity induced by metal–$A\beta$ and metal-free $A\beta$, and the interactions between $A\beta$ species and cell membranes. As displayed in Fig. 6a, $A\beta$ species preincubated with SST for 1, 8 and 24 h in the absence and presence of metal ions were introduced to human neuroblastoma SH-SY5Y cells for 24 h. Cu(II)–$A\beta_{42}$ and Zn(II)–$A\beta_{42}$ pretreated with SST for 8 and 24 h improved cell survival by ~20% and ~10%, respectively; however, the 1 h preincubation was not enough to recover their toxicity (Fig. 6b). As expected from the aggregation results, SST could not significantly affect the cytotoxicity triggered by metal-free $A\beta_{42}$. The cytotoxicity of both metal–$A\beta_{40}$ and metal-free $A\beta_{40}$ was not altered even with addition of SST, as presented in Supplementary Fig. 20. Note that SST is relatively stable for 24 h under our experimental conditions that were used in Abs and CD spectroscopic studies (Fig. 2c and Supplementary Fig. 20d).

To identify a relationship between the decrease in the cytotoxicity of Cu(II)–$A\beta_{42}$ and Zn(II)–$A\beta_{42}$ by SST and their interactions with cell membranes, we carried out immunocytochemistry studies in SH-SY5Y cells that can uptake $A\beta$ species[47]. After treating cells with SST-free and SST-added metal–$A\beta$ and metal-free $A\beta$, cellular membranes were stained with a fluorescent membrane dye followed by labelling $A\beta$ species using a fluorophore-conjugated antibody, as illustrated in Fig. 6c and Supplementary Figs. 21–23. The co-localization of two probes for detecting cellular membranes and $A\beta$, respectively, was then quantified by the Manders' coefficient[53]. This parameter can provide the fraction of one probe (for $A\beta$ species) coincident with the second probe (for cellular membranes); therefore, the co-localization of the quantity of interest can be verified. The Manders' coefficients for the species Cu(II)–$A\beta_{42}$ and Zn(II)–$A\beta_{42}$ were calculated to be 0.45 ± 0.02 and 0.55 ± 0.04, respectively, as shown in Fig. 6c. Upon incubation of SST, these values were noticeably decreased by ~40% and ~50%, respectively, implying the reduced interaction between cell membranes and metal–$A\beta_{42}$ species incubated with SST. The localization of metal-free $A\beta_{42}$ species was not modified even with SST, as expected from the cell viability studies. The Manders' coefficients for the metal–$A\beta_{40}$ and metal-free $A\beta_{40}$ with or without SST were almost identical (Supplementary Fig. 22). In summary, these observations suggest that the interactions between metal–$A\beta_{42}$ species and cellular membranes were notably influenced by SST, which may be correlated to the results obtained from the in vitro aggregation and cell-viability investigations.

Conclusion
Impaired neurotransmission is associated with cognitive decline upon the progression of AD[1,6–9]. Misfolded $A\beta$ aggregates found in the AD-affected brain can cause synaptic dysfunction: (1) blocking the receptors; (2) aberrantly releasing neurotransmitters; and

(3) trapping neurotransmitters into senile plaques at the synaptic cleft[10,13,15,47]. The mechanisms by which direct interactions with pathogenic factors can alter the structures and functions of neurotransmitters remain unknown. Our studies demonstrate that the interactions of SST with Cu(II), Cu(II)–/Zn(II)–$A\beta$ and metal-free $A\beta$ can direct the self-assembly of SST. Cu(II) binding to SST contributes to the alignment of the disulfide bond and compacts the N-terminal region to induce its aggregation. In the case of $A\beta$, it can form a heterodimer and a ternary complex with SST in the absence and presence of metal ions, respectively, and induce the aggregation of SST possibly through electrostatic interactions. The ability of SST aggregates produced by Cu(II), metal–$A\beta$ and metal-free $A\beta$ to bind to the GPCR is lower than monomeric SST in living cells. Thus, SST is conformationally changed and, consequently, loses its normal function as a neurotransmitter in the presence of these pathogenic elements. In a reverse direction, SST noticeably modifies the aggregation of metal–$A\beta$ and the morphology of the resultant aggregates. The interactions between metal–$A\beta_{42}$ aggregates incubated with SST and cellular membranes are reduced, leading to their decreased cytotoxicity. These observations support a gain of modulative function of SST against metal–$A\beta$. Moreover, we probed the aforementioned effects employing a SST isoform and an $A\beta$ fragment. As depicted in Supplementary Fig. 24, SST28, another biologically active SST isoform produced by proteolytically cleaving preprosomatostatin[23], could alter the aggregation of metal-treated $A\beta_{40}$ and $A\beta_{42}$. Furthermore, $A\beta_{25–35}$, found in senile plaques as the shortest $A\beta$-derived fragment that aggregates exhibiting β-sheet fibrils and triggers the cytotoxicity observed with full-length $A\beta$[54], was able to induce the aggregation of SST, but its cytotoxicity could not be recovered by treatment with SST (Supplementary Fig. 25). The mechanisms of such effects will be further identified in the near future.

As additional future plans, the structures of metal(SST) complexes and their impact on $A\beta$ aggregation and toxicity through their contacts in vivo can be continuously analysed based on observations from our solution and cell studies. The in vivo investigations would be challenging due to the heterogeneous nature (for example, conformation, distribution) of SST, metal ions and $A\beta$ in the brain; thus, we will carefully design and conduct experiments with the proper selection of animal models. Overall, this work describes a loss of normal function and a gain of modulative function of a native neuropeptide, SST, through intermolecular interactions with pathogenic elements found in AD. Our studies illuminate that the structure and activity of SST are variable under pathological conditions, which provides broader insight into the roles of neuropeptides in the pathologies of neurodegenerative diseases.

Online content
Any methods, additional references, Nature Research reporting summaries, source data, extended data, supplementary information, acknowledgements, peer review information; details of author contributions and competing interests; and statements of data and code availability are available at https://doi.org/10.1038/s41557-022-00984-3.

References
1. Lemoine, D. et al. Ligand-gated ion channels: new insights into neurological disorders and ligand recognition. *Chem. Rev.* **112**, 6285–6318 (2012).
2. Ng, J., Papandreou, A., Heales, S. J. & Kurian, M. A. Monoamine neurotransmitter disorders—clinical advances and future perspectives. *Nat. Rev. Neurol.* **11**, 567–584 (2015).
3. Jacob, T. C., Moss, S. J. & Jurd, R. GABA$_A$ receptor trafficking and its role in the dynamic modulation of neuronal inhibition. *Nat. Rev. Neurosci.* **9**, 331–343 (2008).

4. Hyman, S. E. Neurotransmitters. *Curr. Biol.* **15**, R154–R158 (2005).

5. Dorsam, R. T. & Gutkind, J. S. G-protein-coupled receptors and cancer. *Nat. Rev. Cancer* **7**, 79–94 (2007).

6. Xu, Y. et al. Neurotransmitter receptors and cognitive dysfunction in Alzheimer's disease and Parkinson's disease. *Prog. Neurobiol.* **97**, 1–13 (2012).

7. Kepp, K. P. Bioinorganic chemistry of Alzheimer's disease. *Chem. Rev.* **112**, 5193–5239 (2012).

8. Savelieff, M. G. et al. Development of multifunctional molecules as potential therapeutic candidates for Alzheimer's disease, Parkinson's disease, and amyotrophic lateral sclerosis in the last decade. *Chem. Rev.* **119**, 1221–1322 (2019).

9. Kashyap, G. et al. Synapse loss and progress of Alzheimer's disease—a network model. *Sci. Rep.* **9**, 6555 (2019).

10. Nam, E., Nam, G. & Lim, M. H. Synaptic copper, amyloid-β, and neurotransmitters in Alzheimer's disease. *Biochemistry* **59**, 15–17 (2020).

11. Forner, S., Baglietto-Vargas, D., Martini, A. C., Trujillo-Estrada, L. & LaFerla, F. M. Synaptic impairment in Alzheimer's disease: a dysregulated symphony. *Trends Neurosci.* **40**, 347–357 (2017).

12. Miller, L. M. et al. Synchrotron-based infrared and X-ray imaging shows focalized accumulation of Cu and Zn co-localized with β-amyloid deposits in Alzheimer's disease. *J. Struct. Biol.* **155**, 30–37 (2006).

13. Lee, S. J. C., Nam, E., Lee, H. J., Savelieff, M. G. & Lim, M. H. Towards an understanding of amyloid-β oligomers: characterization, toxicity mechanisms, and inhibitors. *Chem. Soc. Rev.* **46**, 310–323 (2017).

14. Larson, M. E. & Lesné, S. E. Soluble Aβ oligomer production and toxicity. *J. Neurochem.* **120**, 125–139 (2012).

15. Zhao, Y. et al. Amyloid beta peptides block new synapse assembly by Nogo receptor-mediated inhibition of T-type calcium channels. *Neuron* **96**, 355–372 (2017).

16. Hung, Y. H., Bush, A. I. & Cherny, R. A. Copper in the brain and Alzheimer's disease. *J. Biol. Inorg. Chem.* **15**, 61–76 (2010).

17. Kepp, K. P. & Squitti, R. Copper imbalance in Alzheimer's disease: convergence of the chemistry and the clinic. *Coord. Chem. Rev.* **397**, 168–187 (2019).

18. Faller, P. Copper and zinc binding to amyloid-β: coordination, dynamics, aggregation, reactivity and metal-ion transfer. *ChemBioChem* **10**, 2837–2845 (2009).

19. Noy, D. et al. Zinc–amyloid β interactions on a millisecond time-scale stabilize non-fibrillar Alzheimer-related species. *J. Am. Chem. Soc.* **130**, 1376–1383 (2008).

20. Faller, P., Hureau, C. & Berthoumieu, O. Role of metal ions in the self-assembly of the Alzheimer's amyloid-β peptide. *Inorg. Chem.* **52**, 12193–12206 (2013).

21. Kepp, K. P. Alzheimer's disease: how metal ions define β-amyloid function. *Coord. Chem. Rev.* **351**, 127–159 (2017).

22. Han, J., Du, Z. & Lim, M. H. Mechanistic insight into the design of chemical tools to control multiple pathogenic features in Alzheimer's disease. *Acc. Chen. Res.* **54**, 3930–3940 (2021).

23. Patel, Y. C., Liu, J., Galanopoulou, A. & Parachristou, C. N. *Handbook of Physiology: Section 7: The Endocrine System* (Oxford Univ. Press, 2001).

24. Willén, K., Sroka, A., Takahashi, R. H. & Gouras, G. K. Heterogeneous association of Alzheimer's disease-linked amyloid-β and amyloid-β protein precursor with synapses. *J. Alzheimers Dis.* **60**, 511–524 (2017).

25. Saiz-Sanchez, D., De la Rosa-Preito, C., Ubeda-Banon, I. & Martinez-Marcos, A. Interneurons, tau and amyloid-β in the piriform cortex in Alzheimer's disease. *Brain Struct. Funct.* **220**, 2011–2025 (2015).

26. Weckbecker, G. et al. Opportunities in somatostatin research: biological, chemical and therapeutic aspects. *Nat. Rev. Drug Discov.* **2**, 999–1017 (2003).

27. Song, Y.-H., Yoon, J. & Lee, S.-H. The role of neuropeptide somatostatin in the brain and its application in treating neurological disorders. *Exp. Mol. Med.* **53**, 328–338 (2021).

28. Jayasekharan, T., Gupta, S. L. & Dhiman, V. Binding of Cu+ and Cu2+ with peptides: peptides = oxytocin, Arg8-vasopressin, bradykinin, angiotensin-I, substance-P, somatostatin, and neurotensin. *J. Mass Spectrom.* **53**, 296–313 (2018).

29. Wang, H. et al. Somatostatin binds to the human amyloid β peptide and favors the formation of distinct oligomers. *eLife* **6**, e28401 (2017).

30. Solarski, M., Wang, H., Wille, H. & Schmitt-Ulms, G. Somatostatin in Alzheimer's disease: a new role for an old player. *Prion* **12**, 1–8 (2018).

31. Saito, T. et al. Somatostatin regulates brain amyloid β peptide Aβ42 through modulation of proteolytic degradation. *Nat. Med.* **11**, 434–439 (2005).

32. Anoop, A. et al. Elucidating the role of disulfide bond on amyloid formation and fibril reversibility of somatostatin-14: relevance to its storage and secretion. *J. Biol. Chem.* **289**, 16884–16903 (2014).

33. Dharmadana, D., Reynolds, N. P., Dekiwadia, C., Conn, C. E. & Valéry, C. Heparin assisted assembly of somatostatin amyloid nanofibrils results in disordered precipitates by hindrance of protofilaments interactions. *Nanoscale* **10**, 18195–18204 (2018).

34. Meng, X. et al. Stable H3 peptide was delivered by gold nanorods to inhibit LSD1 activation and induce human mesenchymal stem cells differentiation. *Oncotarget* **8**, 23110–23119 (2017).

35. Kahn, P. C. & Beychok, S. Far-ultraviolet optical activity of crystals in mulls. I. Cystine. *J. Am. Chem. Soc.* **90**, 4168–4170 (1968).

36. Wang, H., Qian, T., Zhao, Y. & Li, Y. A toolkit of highly selective and sensitive genetically encoded neuropeptide sensors. Preprint at https://doi.org/10.1101/2022.03.26.485911 (2022).

37. Feng, J. et al. A genetically encoded fluorescent sensor for rapid and specific in vivo detection of norepinephrine. *Neuron* **102**, 745–761 (2019).

38. Jing, M. et al. An optimized acetylcholine sensor for monitoring in vivo cholinergic activity. *Nat. Methods* **17**, 1139–1146 (2020).

39. Pratesi, A. et al. DOTA-derivatives of octreotide dicarba-analogs with high affinity for somatostatin sst2,5 receptors. *Front. Chem.* **5**, 8 (2017).

40. Vivian, J. T. & Callis, P. R. Mechanisms of tryptophan fluorescence shifts in proteins. *Biophys. J.* **80**, 2093–2109 (2001).

41. Thordarson, P. Determining association constants from titration experiments in supramolecular chemistry. *Chem. Soc. Rev.* **40**, 1305–1323 (2011).

42. Yang, W., Chen, X., Su, H., Fang, W. & Zhang, Y. The fluorescence regulation mechanism of the paramagnetic metal in a biological HNO sensor. *Chem. Commun.* **51**, 9616–9619 (2015).

43. Ćendić, M. et al. Chelating properties of EDTA-type ligands containing six-membered backbone ring toward copper ion: structure, EPR and TD-DFT evaluation. *Polyhedron* **124**, 215–228 (2017).

44. van Grondelle, W. et al. Lamination and spherulite-like compaction of a hormone's native amyloid-like nanofibrils: spectroscopic insights into key interactions. *Faraday Discuss.* **166**, 163–180 (2013).

45. Kocyła, A., Pomorski, A. & Krężel, A. Molar absorption coefficients and stability constants of Zincon metal complexes for determination of metal ions and bioinorganic applications. *J. Inorg. Biochem.* **176**, 53–65 (2017).

46. Vivekanandan, S., Brender, J. R., Lee, S. Y. & Ramamoorthy, A. A partially folded structure of amyloid-beta(1-40) in an aqueous environment. *Biochem. Biophys. Res. Commun.* **411**, 312–316 (2011).

47. Hu, X. et al. Amyloid seeds formed by cellular uptake, concentration, and aggregation of the amyloid-beta peptide. *Proc. Natl Acad. Sci. USA* **106**, 20324–20329 (2009).

48. Biancalana, M. & Koide, S. Molecular mechanism of thioflavin-T binding to amyloid fibrils. *Biochim. Biophys. Acta* **1804**, 1405–1412 (2010).

49. Baghallab, I., Reyes-Ruiz, J. M., Abulnaja, K., Huwait, E. & Glabe, C. Epitomic characterization of the specificity of the anti-amyloid Aβ monoclonal antibodies 6E10 and 4G8. *J. Alzheimers Dis.* **66**, 1235–1244 (2018).

50. Bernstein, S. L. et al. Amyloid-β protein oligomerization and the importance of tetramers and dodecamers in the aetiology of Alzheimer's disease. *Nat. Chem.* **1**, 326–331 (2009).

51. Nirmalraj, P. N. et al. Complete aggregation pathway of amyloid β (1-40) and (1-42) resolved on an atomically clean interface. *Sci. Adv.* **6**, eaaz6014 (2020).

52. Benilova, I., Karran, E. & De Strooper, B. The toxic Aβ oligomer and Alzheimer's disease: an emperor in need of clothes. *Nat. Neurosci.* **15**, 349–357 (2012).

53. Dunn, K. W., Kamocka, M. M. & McDonald, J. H. A practical guide to evaluating colocalization in biological microscopy. *Am. J. Physiol. Cell Physiol.* **300**, C723–C742 (2011).

54. Clementi, M. E. et al. Aβ(31-35) and Aβ(25-35) fragments of amyloid beta-protein induce cellular death through apoptotic signals: role of the redox state of methionine-35. *FEBS Lett.* **579**, 2913–2918 (2005).

Methods

Materials. All chemical reagents were purchased from commercial suppliers and used as received unless otherwise stated. Synthetic SST (AGCKNFFWKTFTSC), SST28 (SANSNPAMAPRERKAGCKNFFWKTFTSC) and Aβ$_{25-35}$ (GSNKGAIIGLM) were purchased from Sigma-Aldrich. Synthetic Aβ$_{40}$ (DAEFRHDSGYEVHHQKLVFFAEDVGSNKGAIIGLMVGGVV) and Aβ$_{42}$ (DAEFRHDSGYEVHHQKLVFFAEDVGSNKGAIIGLMVGGVVIA) were obtained from Peptide Institute and were purified by HPLC using YMC Pack ODS-A (YMC) and Agilent ZORBAX 300SB-C18 columns (Agilent), respectively. HEPES (2-(4-(2-hydroxyethyl)piperazin-1-yl)ethanesulfonic acid) was purchased from Sigma-Aldrich. The buffered solution was prepared in doubly distilled water (ddH$_2$O; Milli-Q Direct 16 system (18.2 MΩ·cm; Merck). Trace metal contamination was removed from all solutions used for experiments by treating with Chelex (Sigma-Aldrich) overnight. The Abs spectra were recorded on an Agilent 8453 ultraviolet−visible spectrophotometer (Agilent). Images obtained by gel/Western blot were visualized by a ChemiDoc MP imaging system (Bio-Rad). The secondary structures of SST were analysed by a JASCO-815 150-L CD spectropolarimeter (Jasco; KAIST Analysis Center for Research Advancement (KARA)). The absorbance and fluorescence values were determined by a SpectraMax M5 microplate reader (Molecular Devices) and a HORIBA QuantaMaster QM 400 spectrophotometer (HORIBA; KARA). Live-cell imaging experiments were conducted with a Zeiss ApoTome2.0 (Carl Zeiss). X-band continuous-wave (CW)-EPR spectra were obtained with a Bruker EMXplus EPR spectrometer (Bruker BioSpin) equipped with an ER 4141VT digital temperature control system (Bruker BioSpin) and an ER 4119HS cavity (Bruker BioSpin). A JASCO J-1500 CD spectrometer was used for collecting MCD spectra (Jasco). The MCD spectra were measured in the solenoid core bore of a Cryomagnetics 5 T cryogen-free superconducting magnet, providing a longitudinal magnetic field up to ± 5 T parallel to the light propagation direction. ESI–MS experiments were performed by an Agilent 6530 Accurate Mass Quadrupole Time-of-Flight (Q-TOF) mass spectrometer with an ESI source (Agilent). Morphologies of Aβ aggregates produced from aggregation experiments were taken on a Tecnai F20 transmission electron microscope (FEI; KARA). Confocal microscopic images were taken with a Zeiss LSM 880 (Carl Zeiss; KARA).

Preparation of SST and Aβ. SST and Aβ were dissolved in ddH$_2$O and NH$_4$OH (1% w/w, aq.; Sigma-Aldrich), respectively. The resultant solutions were aliquoted, lyophilized overnight and stored at −80 °C. A stock solution of SST was prepared by dissolving the lyophilized peptide with ddH$_2$O. A stock solution of Aβ was prepared by dissolving the lyophilized peptide with NH$_4$OH (1% w/w, aq.) followed by addition of ddH$_2$O, as previously reported[55]. The concentration of the peptide solution was determined by measuring the absorbance at 280 nm (for SST, $\varepsilon = 5{,}690\,M^{-1}\,cm^{-1}$; for SST28, $\varepsilon = 5{,}625\,M^{-1}\,cm^{-1}$; for Aβ$_{40}$, $\varepsilon = 1{,}450\,M^{-1}\,cm^{-1}$; for Aβ$_{42}$, $\varepsilon = 1{,}490\,M^{-1}\,cm^{-1}$). The concentration of Aβ$_{25-35}$ that lacks aromatic amino acid residues was assessed by measuring the absorbance at 214 nm ($\varepsilon = 10{,}651\,M^{-1}\,cm^{-1}$).

Gel/Western blot. SST or SST28 (100 μM) was incubated with metal ions (CuCl$_2$ or ZnCl$_2$; 100 μM) for 5 min, 1 h, 8 h and 24 h at 37 °C with constant agitation (250 r.p.m.) in 20 mM HEPES, pH 7.4, 150 mM NaCl. In a similar manner, SST (100 μM) and Aβ (100 μM) were coincubated with or without metal ions (100 μM) in the buffered solution for 5 min, 1 h, 8 h and 24 h at 37 °C with constant agitation (250 r.p.m.). To analyse the aggregation of SST in the presence of Cu(II) under anaerobic conditions, SST (100 μM) was incubated with CuCl$_2$ (100 μM) for 24 h in 20 mM HEPES, pH 7.4, 150 mM NaCl under nitrogen gas at room temperature with no agitation. The samples were prepared using Eppendorf tubes. The resultant peptide species were analysed by gel/Western blot using an anti-SST antibody (Enzo Life Science) or an anti-Aβ antibody (6E10; Biolegend)[55]. Each sample (10 μL) was separated onto a tricine gel (10–20% w/v acrylamide; Invitrogen). For the SDS–PAGE, each sample (10 μL) was denatured with urea (8 M, 4 μL; TCI Chemicals) for 15 min and resolved through the homemade gel (6% w/v acrylamide for stacking gels; 18% w/v acrylamide for resolving gels; 0.1% w/v SDS; non-reducing conditions)[56].

Following separation, the peptides were transferred onto nitrocellulose membranes and blocked with bovine serum albumin (BSA, 3% w/v; Sigma-Aldrich) in Tris-buffered saline (TBS) containing 0.1% v/v Tween-20 (Sigma-Aldrich) (TBS-T) for 3 h at room temperature or overnight at 4 °C. The membranes were incubated with anti-SST (1:8,000) or 6E10 (1:2,000) in a solution of BSA (2% w/v in TBS-T) overnight at room temperature. After washing with TBS-T three times (10 min), a horseradish-peroxidase-conjugated goat anti-rabbit secondary antibody (1:2,500 for anti-SST; Promega) or the goat anti-mouse secondary antibody (1:5,000 for 6E10; Cayman) in a solution of BSA (2% w/v in TBS-T) was added for 2 h at room temperature. A homemade ECL kit[57] was used to visualize the images gained by gel/Western blot on a ChemiDoc MP Imaging System (Bio-Rad). The measurements were conducted in triplicate.

CD spectroscopy. The secondary structures of SST were analysed by CD spectroscopy[58,59]. SST (100 μM) was incubated in the absence and presence of Cu(NO$_3$)$_2$·nH$_2$O or Zn(NO$_3$)$_2$·nH$_2$O (100 μM) in 20 mM HEPES, pH 7.4, 150 mM

NaF. The samples were incubated at 37 °C with constant agitation (250 r.p.m.). The samples were prepared using Eppendorf tubes. CD spectra of the samples were collected in the range from 200 to 260 nm with a cell path length of 0.5 mm. The digital integration time, the bandwidth and the scanning speed were 4 s, 2 nm and 20 nm min^{-1}, respectively. Each spectrum was smoothed by Fourier transforms. The measurements were conducted in triplicate.

Receptor-binding studies. The human embryonic kidney (HEK293T) cells were purchased from the American Type Culture Collection (ATCC). Cells were maintained in Dulbecco's modified Eagle's medium (DMEM; HyClone) supplemented with 10% v/v fetal bovine serum (FBS; HyClone) and 1% v/v penicillin/streptomycin (HyClone). The cells were grown and maintained at 37 °C in a humidified atmosphere with 5% CO$_2$. The GRAB$_{SST}$ sensor has been developed based on human SST receptor type 5 (SSTR5) following previously reported methods[36]. For the GRAB$_{SST}$ sensor (GRAB-SST1.0) expression, HEK293T cells were plated on a glass-bottomed dish (SPL) precoated with poly-D-lysine hydrobromide (Sigma-Aldrich) at a density of approximately 500,000 cells mL^{-1} in DMEM supplemented with 10% v/v FBS (without the antibiotics) and grown for 24 h. When cells were grown to 80% confluency, they were transfected with the GRAB$_{SST}$ sensor plasmid (pAAV-hsyn-GRAB-SST1.0) using Lipofectamine 2000 (Invitrogen) and incubated for 24 h. The culture medium was replaced with Tyrode's solution (10 mM HEPES, pH 7.3–7.4, 150 mM NaCl, 4 mM KCl, 2 mM MgCl$_2$, 2 mM CaCl$_2$, 10 mM glucose) before the imaging experiments. Various concentrations of samples were applied manually into the culture dish while imaging the cells at a rate of 0.1 Hz. GFP fluorescence emitted from the GRAB$_{SST}$ sensor-expressing cells (GRAB-SST1.0 expression for 24 h) upon binding to SST were imaged by the fluorescent microscope equipped with a 40× oil-immersion objective, 488 nm laser and 500–550 nm emission filter (Zeiss Apotome 2.0; Carl Zeiss). To obtain the effective concentration (EC$_{50}$) value of the GRAB$_{SST}$ sensor against SST, various concentrations of SST (0.003, 0.01, 0.03, 0.05, 0.1, 0.3, 0.5, 1, 3 and 7 μM; 20 mM HEPES, pH 7.4; 150 mM NaCl) were sequentially titrated with the cells at 1 min intervals. The change in fluorescence ($\Delta F/F_0$) was plotted as a function of log[SST]. The EC$_{50}$ value was determined to be ~0.74 μM by a dose–response curve-fitting using equation (1). F_i and F_f indicate the fluorescence intensity of initial and final points at plateaus, respectively, while p refers to the slope factor.

$$\frac{\Delta F}{F_{max}} = F_i + \frac{F_f - F_i}{1 + 10^{\log(EC_{50} - x)p}} \tag{1}$$

SST (100 μM) was incubated with or without metal chlorides (100 μM) in the absence and presence of Aβ$_{40}$ (100 μM) for 24 h at 37 °C with constant agitation (250 rpm) in 20 mM HEPES, pH 7.4, 150 mM NaCl. The samples were prepared using Eppendorf tubes. On the assumption that the EC$_{50}$ value of the GRAB$_{SST}$ sensor is <1 μM, the preincubated samples were further diluted to 38 μM with the buffered solution and mixed with the cell medium (1.3% v/v) at the final concentration of 0.5 μM. For the quantitative analysis of the green fluorescence changes, the mean grey values in the imaged cells were calculated by ImageJ v.1.53k software. The baseline fluorescence value (F_0) was computed by averaging the difference in the fluorescence intensity between the region of interest (ROI) (F_{ROI}) and the background (F_{BG}) before treatment of the samples in the cells. We calculated the fluorescence changes with treatment of the samples in the cells that showed F_0 in the range of 50–200. The difference in the GRAB$_{SST}$ fluorescence levels ($\Delta F/F_0$, where $\Delta F = (F_{ROI} - F_{BG}) - F_0$) at the time point 3 min after treatment of the samples was averaged and presented with the s.e.m. ($n = 10–21$). Statistical evaluation of the difference in receptor binding among test groups was performed by Kruskal–Wallis test with Bonferroni correction with significance set at $P = 0.05$ (IBM SPSS).

Trp fluorescence quenching studies. SST (100 μM) was treated with or without metal ions (CuCl$_2$ and ZnCl$_2$; 100 μM) in 20 mM HEPES, pH 7.4, 150 mM NaCl. The samples were incubated for 5 min and 24 h at 37 °C with constant agitation (250 r.p.m.). The samples were prepared using Eppendorf tubes. Fluorescence spectra of the samples were recorded by a microplate reader (Molecular Devices; $\lambda_{ex} = 280$ nm; $\lambda_{em} = 300–500$ nm). The measurements were performed in triplicate.

Measurements of the K_ds. The K_d values for the M(II)(SST) complexes were measured by fluorescence and ultraviolet–visible spectroscopy, respectively. Various concentrations of CuCl$_2$ or Cu(NO$_3$)$_2$·nH$_2$O were titrated into a solution of SST (100 μM) in 20 mM HEPES, pH 7.4. Upon treatment with Cu(II), the intrinsic fluorescence of SST was quenched ($\lambda_{ex} = 280$ nm; $\lambda_{em} = 300–500$ nm). The change in the fluorescence was plotted as a function of [Cu(II)]. The plot was then fitted using equation (2) to obtain the K_d value of SST for Cu(II)[41]. It should be noted that ΔF and ΔF_0 represent the difference in the integrated emission intensity from 300 to 500 nm and its maximum value, respectively. The measurements were conducted in triplicate. Thereafter, the K_d value for Cu(II)(SST) was calculated using a nonlinear curve fitting in OriginPro 9.0 software.

$$\frac{\Delta F}{F_0} = \frac{K_d + [SST]_{total} + [Cu(II)] - \sqrt{(K_d + [SST]_{total} + [Cu(II)])^2 - 4 \times [SST]_{total} \times [Cu(II)]}}{2 \times [SST]_{total}} \tag{2}$$

The K_d value for Zn(II)(SST) was determined by competition experiments employing Zincon (2-carboxy-2′-hydroxy-5′-sulfoformazyl-benzene monosodium salt; Alfa Aesar). The solutions of Zincon (10 μM; 0.4% v/v DMSO) and ZnCl$_2$ or Zn(NO$_3$)$_2$·nH$_2$O (5 μM) were prepared in 20 mM HEPES, pH 7.4. The resultant solution was titrated with SST (5–450 μM). The concentration of Zn(II)(Zincon) was estimated by measuring the absorbance at 618 nm ($\varepsilon = 26{,}200\,\mathrm{M^{-1}\,cm^{-1}}$ at pH 7.4)[45]. The concentration of the Zn(II)-bound SST complex was calculated from mass-balance equations (3)–(6). Thereafter, the K_d value for Zn(II)(SST) was calculated using equation (7), a nonlinear regression on the basis of the Langmuir binding isotherm, in OriginPro 9.0 software. The measurements were conducted in triplicate.

$$\mathrm{Zn(II)(Zincon) + SST \rightleftharpoons Zincon + Zn(II)(SST)} \tag{3}$$

$$\mathrm{[Zincon] = [Zincon]_{total} - [Zn(II)(Zincon)]} \tag{4}$$

$$\mathrm{[Zn(II)(SST)] = [Zn(II)]_{total} - [Zn(II)(Zincon)]} \tag{5}$$

$$\mathrm{[SST] = [SST]_{total} - [Zn(II)(SST)]} \tag{6}$$

$$\mathrm{[Zn(II)(SST)]} = \frac{\mathrm{[SST] \times [Zn(II)]}}{K_d + \mathrm{[SST]}} \tag{7}$$

Abs spectroscopy. The Abs spectra of CuCl$_2$ (100 μM) with or without treatment of EDTA (100 μM) were obtained in 20 mM HEPES, pH 7.4. To further assess the ligand field of SST towards Cu(II), the solution of CuCl$_2$ (100 μM) and SST (100 μM) was prepared in 20 mM HEPES, pH 7.4 and subsequently mixed with EDTA (100 μM).

EPR spectroscopy. The solution of CuCl$_2$ (100 μM) was prepared with either EDTA (100 μM), SST (100 μM) or both in 20 mM HEPES, pH 7.4 and transferred to EPR tubes. The EPR spectra of all frozen samples were recorded with the following experimental parameters: microwave frequency, 9.4 GHz; microwave power, 25 mW; modulation frequency, 100 kHz; modulation amplitude, 5 G; time constant, 0.01 ms; conversion time, 35 ms; sweep time, 120 s; number of scans, 4; temperature, 100 K. All the EPR spectra were simulated with the W95EPR program developed by F. Neese.

Computational details. The Gaussian 09-d.01 package[60] was used for geometry optimizations and time-dependent density functional theory (TDDFT)[61] calculations, while EPR parameters[62] were calculated with ORCA 4.2.0 software[63,64]. The initial geometries of [Cu(EDTA)]$^{2-}$ and [Cu(HEDTA)]$^-$ complexes were obtained from X-ray crystal structures and water molecules were introduced in consideration of hydrogen bonds[43]. The NMR-predicted structure of SST (PDB 2MI1[32]) was utilized to construct the Cu(II)-bound SST models. The N-terminal primary amine (Ala1), the C-terminal carboxylate group (Cys14), and the ε-amino group of Lys4 and Lys9 were chosen for possible Cu(II)-binding sites, and water molecules were added to complete the coordination sphere of the Cu(II) site. Geometry optimizations were performed with the BP86 functional[65,66], the 6-31g(d) basis set[67–71], and the PCM (water) solvation model[72]. For the TDDFT and EPR parameter calculations, the optimized structures were truncated to include the Cu(II) centre and the ligands up to the second coordination sphere, and capped with hydrogen atoms that were placed at a distance of 1.1 Å from neighbouring carbon atoms and then geometry-optimized. The B3LYP functional[73] and the 6-31g(d) basis set were used for the TDDFT and EPR parameter calculations, while for the latter, the Cu(II) centre and the coordinated nitrogen and oxygen donor atoms were treated with the CP(PPP)[74] and EPR-III[75] basis sets, respectively.

ESI–MS. SST (100 μM) was incubated with Aβ (100 μM) in the absence and presence of CuCl$_2$ or ZnCl$_2$ (100 μM) for 3 h at 37 °C with constant agitation (250 r.p.m.) in 20 mM ammonium acetate. The samples were prepared using Eppendorf tubes. Before injection into the mass spectrometer, the resultant samples were diluted 10-fold with LC-grade H$_2$O. The capillary voltage, the drying gas flow and the gas temperature were set to 5.8 kV, 12 L min^{-1} and 300 °C, respectively. The ESI parameters and experimental conditions for ESI–MS^2 were the same as above. The collision-induced dissociation was conducted by applying the collision energy at 55 eV. The measurements were conducted in triplicate.

Docking studies. Docking studies of SST (PDB 2MI1[32]) against Aβ$_{40}$ monomer (PDB 2LFM[46]) were conducted with AutoDock Vina v.1.2.0[76]. The structures of SST and Aβ$_{40}$ were prepared through AutoDock Tools and imported into PyRx, which was used to run AutoDock Vina[76]. The exhaustiveness for the docking runs was set at 1,024. The docked models of SST with Aβ$_{40}$ were visualized using Pymol 2.0.7. The conformers ($\Delta G < -11.0\,\mathrm{kcal\,mol^{-1}}$) in the two models of SST docked to Aβ$_{40}$ were analysed.

ThT assay. Aβ (20 μM), metal ions (18 μM for CuCl$_2$; 20 μM for ZnCl$_2$) and SST (10, 20, and 100 μM) were incubated with ThT (20 μM) at 37 °C with constant agitation in 20 mM HEPES, pH 7.4, 150 mM NaCl. The samples were prepared using Eppendorf tubes. The fluorescence intensity was measured with a microplate reader (Molecular Devices; $\lambda_{ex} = 440\,\mathrm{nm}$; $\lambda_{em} = 490\,\mathrm{nm}$). The kinetic parameters of Aβ aggregation in the absence and presence of Cu(II) were acquired by fitting the emission curves using a modified Boltzmann-sigmoidal equation (8) in OriginPro 9.0 software[77]. In the case of Zn(II)-added Aβ, the emission curves were fitted by a hyperbolic function using equation (9)[78]. F_i and F_f indicate the fluorescence intensity of initial and final time points, respectively, while k refers the rate constant for the elongation of Aβ aggregation. The $t_{1/2}$ value represents the half-time when the ThT emission intensity reaches 50% of its maximum value. Data are presented as mean ± s.e.m. of three independent experiments and the measurements were carried out using Costar 96-well black polystyrene plates (Sigma-Aldrich).

$$F(t) = F_i + \frac{F_f}{1 + e^{k(t - t_{1/2})}} \tag{8}$$

$$F(t) = \frac{At}{t + t_{1/2}} \tag{9}$$

TEM. Samples for TEM were prepared following previously reported methods[55]. Glow-discharged grids (Formvar/Carbon 300-mesh; Electron Microscopy Sciences) were treated with peptide samples (100 μM; 7.5 μL) for 2 min at room temperature. Excess sample was removed using filter paper followed by washing with ddH$_2$O three times. Each grid incubated with uranyl acetate (1% w/v ddH$_2$O; 7.5 μL) for 2 min was blotted off and dried overnight at room temperature. Locations of the samples on the grids were randomly picked, taking more than 20 images per grid.

Cell viability studies. The human neuroblastoma SH-SY5Y cell line was purchased from the ATCC. SH-SY5Y cells were maintained in media containing 50% v/v minimum essential medium (MEM; GIBCO) and 50% v/v F-12 (GIBCO) supplemented with 10% v/v FBS (Sigma-Aldrich) and 100 U mL^{-1} penicillin with 100 mg mL^{-1} streptomycin (GIBCO). The cells were grown and maintained at 37 °C in a humidified atmosphere with 5% CO$_2$. Cell viability was determined by the MTT assay (MTT = 3-(4,5-dimethylthiazol-2-yl)-2,5-diphenyltetrazolium bromide; Biosesang). Aβ$_{40}$, Aβ$_{42}$ or Aβ$_{25–35}$ (100 μM) and SST (100 μM) were preincubated for 1, 8, or 24 h with or without metal chlorides (100 μM) at 37 °C with constant agitation (250 r.p.m.). The samples were prepared using Eppendorf tubes. Cells were seeded in a 96-well plate (10,000 cells per 100 μL) and treated with the samples to make the final concentrations of 10 μM for Aβ, metal ions and SST. After 24 h incubation, MTT (5 mg mL^{-1} in PBS, pH 7.4, GIBCO; 25 μL) was added to each well and the plate was incubated for 4 h at 37 °C. Formazan produced by cells was solubilized using an acidic solution of N,N-dimethylformamide (DMF; pH 4.5, 50% v/v, aq.) and SDS (20% w/v; Wako Chemicals) overnight at room temperature in the dark. Absorbance was measured at 600 nm with a microplate reader (Molecular Devices). Cell viability was calculated, compared to that of the cells treated with an equivalent amount of the buffered solution (20 mM HEPES, pH 7.4, 150 mM NaCl). Data are presented as mean ± s.e.m. of three independent experiments. For statistical analysis, Student's t-test was used.

Immunocytochemistry studies. SH-SY5Y cells were plated on an imaging dish (35 mm; 45,000 cells per 1.5 mL) and incubated for 48 h. Aβ (100 μM) and SST (100 μM) were preincubated in the absence and presence of metal ions (CuCl$_2$ or ZnCl$_2$; 100 μM) for 24 h at 37 °C with constant agitation (250 r.p.m.). The samples were prepared using Eppendorf tubes. Cells were treated with the samples to make the final concentrations of 10 μM for Aβ, metal ions and SST. After 24 h incubation, cellular membranes were stained with the CellBrite green cytoplasmic membrane dye (1:2,000 in growth medium; Biotium) for 30 min. After washing with fresh growth medium two times (5 min), the cells were fixed with 4% w/v formaldehyde (Sigma-Aldrich) in PBS (GIBCO) for 15 min. Following the fixation, cells were blocked with BSA (3% w/v in TBS; Sigma-Aldrich) for 1.5 h at room temperature. The cells were incubated with 6E10 (1:2,000; Biolegend) in the solution of BSA (2% w/v in TBS) for 2 h. After washing with TBS (4×, 5 min), Alexa Fluor 647-goat anti-mouse secondary antibody (1:1,000; Invitrogen) in a solution of BSA (2% w/v in TBS) was added for 1 h at room temperature. The cells were then washed with TBS (4×, 5 min) and stored at 4 °C. At least four randomly selected fields per condition were captured with a Zeiss LSM 880 confocal microscope (KARA). To avoid crosstalk interference between multiple fluorescent channels, fluorescent images were sequentially scanned ($\lambda_{ex} = 488\,\mathrm{nm}$ for a cellular membrane dye; $\lambda_{ex} = 647\,\mathrm{nm}$ for an anti-mouse secondary antibody). A series of the z-stack images was acquired with a 1 μm step size and projected on two-dimensional images by selecting the highest fluorescent intensity from each slice using ZEN blue 3.2 software. The Manders' correlation coefficient was calculated using the Coloc2 plugin in Fiji 2.1.1 software, and is indicative of the co-localization of the quantity of interest, which is completely independent on the signal proportionality[53].

Reporting summary. Further information on research design is available in the Nature Research Reporting Summary linked to this article.

Data availability

All experimental details and data supporting the findings of this study are available within the paper and its Supplementary Information. The data are also available from the corresponding authors upon reasonable request. Source data are provided with this paper.

References

55. Han, J. et al. Mechanistic approaches for chemically modifying the coordination sphere of copper–amyloid-β complexes. *Proc. Natl Acad. Sci. USA* **117**, 5160–5167 (2020).
56. Pithadia, A. S. et al. Reactivity of diphenylpropynone derivatives toward metal-associated amyloid-β species. *Inorg. Chem.* **51**, 12959–12967 (2012).
57. Mruk, D. D. & Cheng, C. Y. Enhanced chemiluminescence (ECL) for routine immunoblotting: an inexpensive alternative to commercially available kits. *Spermatogenesis* **1**, 121–122 (2011).
58. Geenfield, N. J. Using circular dichroism spectra to estimate protein secondary structure. *Nat. Protoc.* **1**, 2876–2890 (2006).
59. Micsonai, A. et al. Accurate secondary structure prediction and fold recognition for circular dichroism spectroscopy. *Proc. Natl Acad. Sci. USA* **112**, E3095–E3103 (2015).
60. Frisch, M. J. et al. Gaussian 09v (Gaussian, 2009).
61. Runge, E. & Gross, E. K. U. Density-functional theory for time-dependent systems. *Phys. Rev. Lett.* **52**, 997–1000 (1984).
62. Neese, F. Prediction of electron paramagnetic resonance *g* values using coupled perturbed Hartree–Fock and Kohn–Sham theory. *J. Chem. Phys.* **115**, 11080–11096 (2001).
63. Neese, F. The ORCA program system. *WIREs Comput. Mol. Sci.* **2**, 73–78 (2012).
64. Neese, F. Software update: the ORCA program system, version 4.0. *WIREs Comput. Mol. Sci.* **8**, 6 (2018).
65. Becke, A. D. Density-functional exchange-energy approximation with correct asymptotic behavior. *Phys. Rev. A* **38**, 3098–3100 (1988).
66. Perdew, J. P. Density-functional approximation for the correlation energy of the inhomogeneous electron gas. *Phys. Rev. B* **33**, 8822–8824 (1986).
67. Ditchfield, R., Hehre, W. J. & Pople, J. A. Self-consistent molecular-orbital methods. IX. An extended Gaussian-type basis for molecular-orbital studies of organic molecules. *J. Chem. Phys.* **54**, 724–728 (1971).
68. Hehre, W. J., Ditchfield, R. & Pople, J. A. Self-consistent molecular orbital methods. XII. Further extensions of Gaussian-type basis sets for use in molecular orbital studies of organic molecules. *J. Chem. Phys.* **56**, 2257–2261 (1972).
69. Hariharan, P. C. & Pople, J. A. The influence of polarization functions on molecular orbital hydrogenation energies. *Theor. Chim. Acta* **28**, 213–222 (1973).
70. Francl, M. M. et al. Self-consistent molecular orbital methods. XXIII. A polarization-type basis set for second-row elements. *J. Chem. Phys.* **77**, 3654–3665 (1982).
71. Rassolov, V. A., Pople, J. A., Ratner, M. A. & Windus, T. L. 6-31G* basis set for atoms K through Zn. *J. Chem. Phys.* **109**, 1223–1229 (1998).
72. Barone, V. & Cossi, M. Quantum calculation of molecular energies and energy gradients in solution by a conductor solvent model. *J. Phys. Chem. A* **102**, 1995–2001 (1998).
73. Lee, C., Yang, W. & Parr, R. G. Development of the Colle–Salvetti correlation-energy formula into a functional of the electron density. *Phys. Rev. B* **37**, 785–789 (1988).
74. Neese, F. Prediction and interpretation of the ^{57}Fe isomer shift in Mössbauer spectra by density functional theory. *Inorg. Chim. Acta* **337**, 181–192 (2002).
75. Rega, N., Cossi, M. & Barone, V. Development and validation of reliable quantum mechanical approaches for the study of free radicals in solution. *J. Chem. Phys.* **105**, 11060–11067 (1996).
76. Trott, O. & Olson, A. J. AutoDock Vina: improving the speed and accuracy of docking with a new scoring function, efficient optimization and multithreading. *J. Comput. Chem.* **31**, 455–461 (2010).
77. Lin, Y. et al. Diverse structural conversion and aggregation pathways of Alzheimer's amyloid-β (1–40). *ACS Nano* **13**, 8766–8783 (2019).
78. Schreiber, A., Fischer, S. & Lang, T. The amyloid precursor protein forms plasmalemmal clusters via its pathogenic amyloid-β domain. *Biophys. J.* **102**, 1411–1417 (2012).

Author contributions

J.H. and M.H.L. designed the research. J.H. performed the spectroscopic measurements (absorbance, fluorescence and CD), PAGE, ESI–MS, docking studies, biochemical assays, TEM and cell studies with data analysis. T.Q. and Y.L. developed the GRAB$_{SST}$ sensor. J.Y. and S.-H.L. designed the GRAB$_{SST}$ imaging experiment and analysed the data. J.S. and K.P. collected and analysed the spectroscopic data and DFT calculation. E.N. contributed to the immunocytochemistry studies. J.H., E.N., K.P., S.-H.L. and M.H.L. wrote the manuscript with input from all authors.

Competing interests

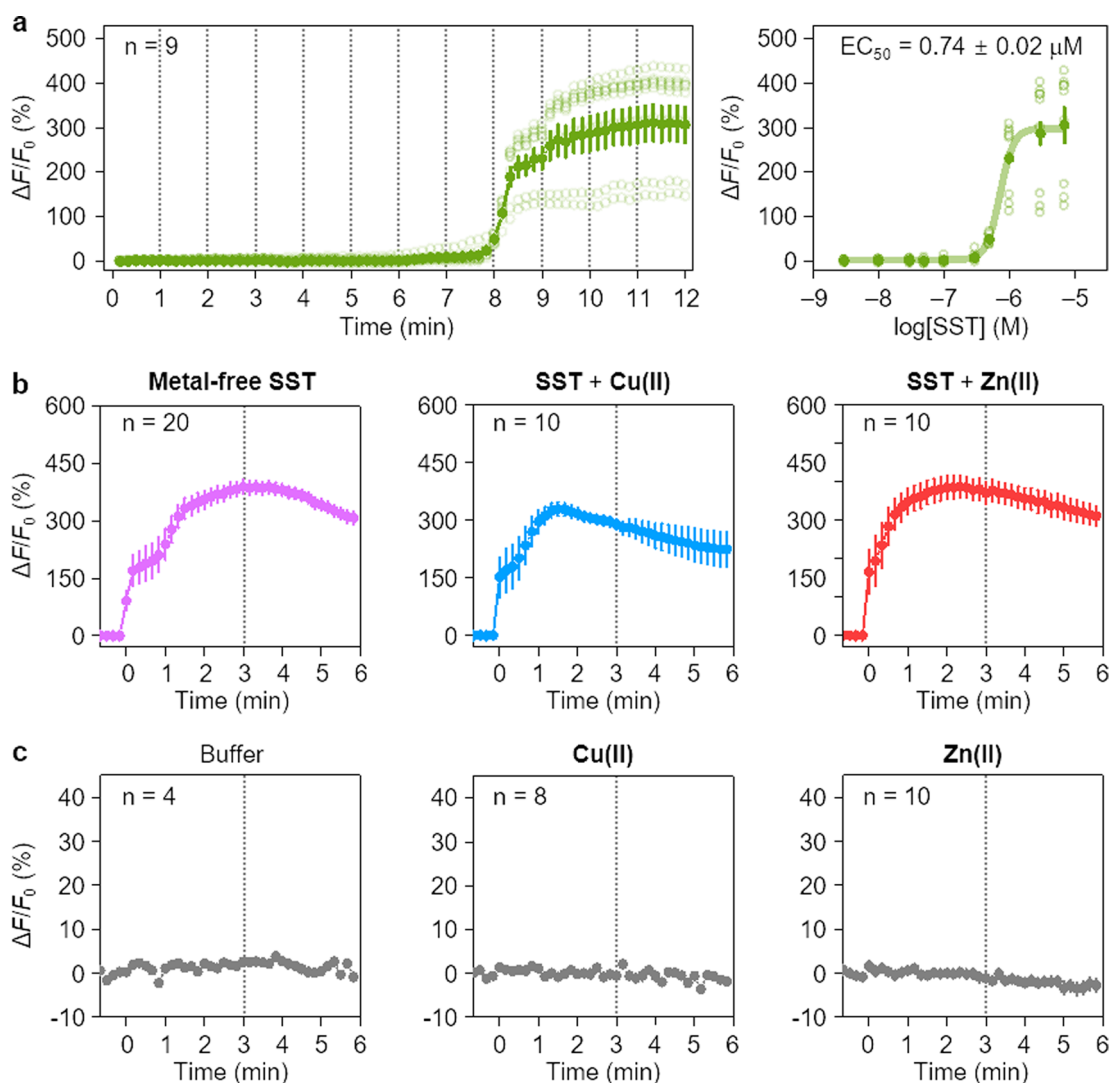The authors declare no competing interests.

Additional information

Extended data is available for this paper at https://doi.org/10.1038/s41557-022-00984-3.

Supplementary information The online version contains supplementary material available at https://doi.org/10.1038/s41557-022-00984-3.
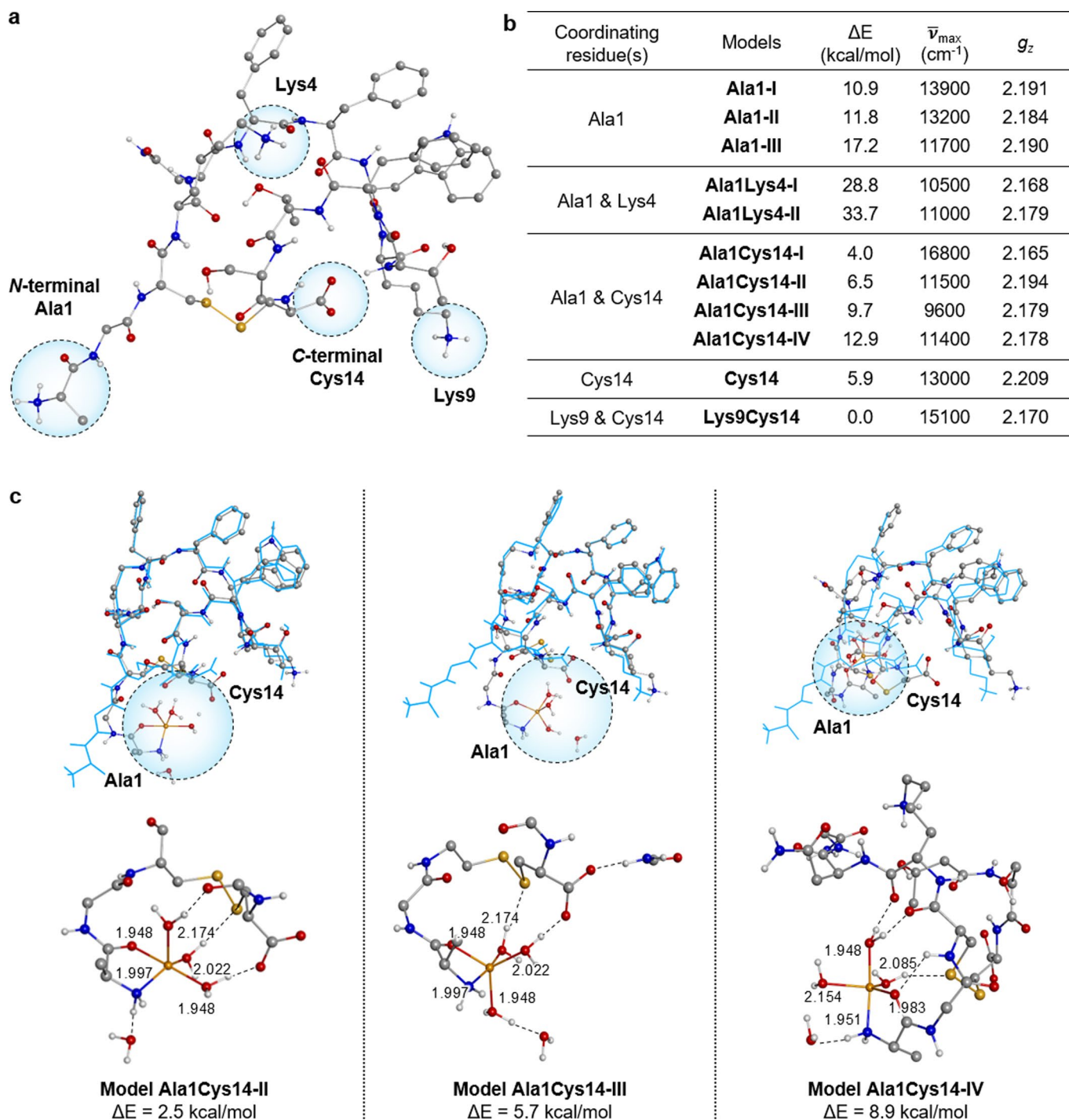
Correspondence and requests for materials should be addressed to Kiyoung Park, Seung-Hee Lee or Mi Hee Lim.

Peer review information *Nature Chemistry* thanks Ujendra Kumar and the other, anonymous, reviewer(s) for their contribution to the peer review of this work.
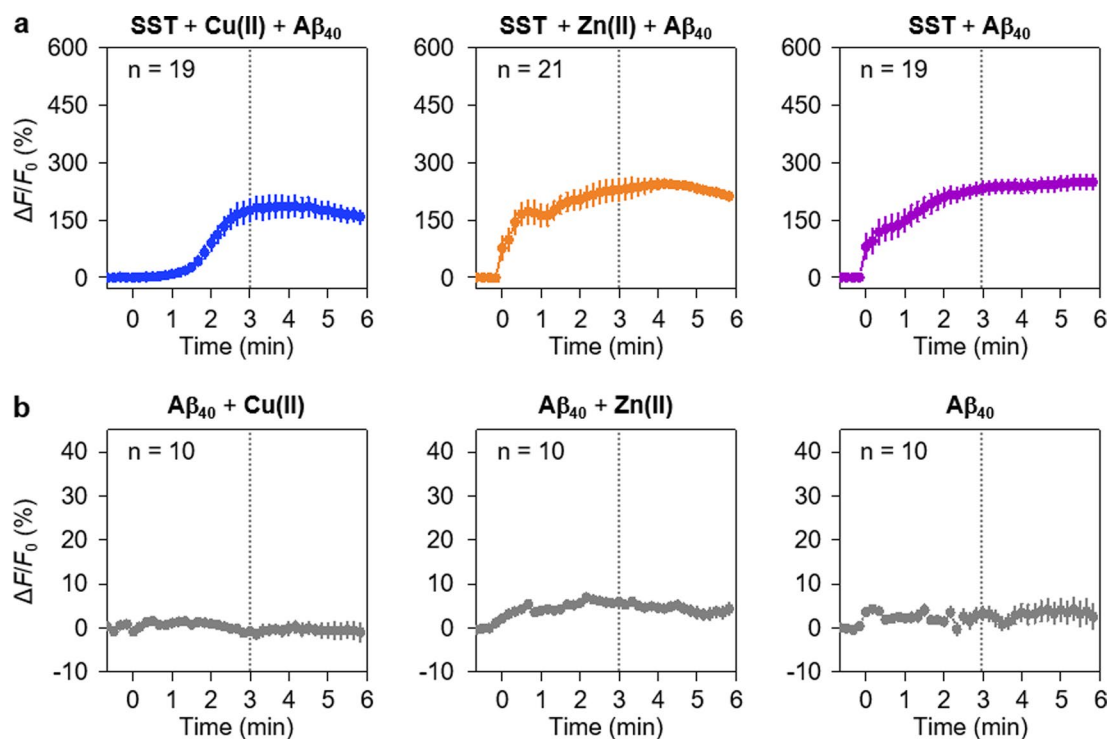
Reprints and permissions information is available at www.nature.com/reprints.

Extended Data Fig. 1 | Receptor-binding studies of SST treated with and without metal ions. a, Titration experiments to determine the EC_{50} value of the $GRAB_{SST}$ sensor against SST. Various concentrations of SST were sequentially added to the $GRAB_{SST}$ sensor-expressing HEK293T cells at a 1 min interval. The $\Delta F/F_0$ values were plotted as a function of log[SST] and fitted to obtain the EC_{50} value. Data are presented as mean ± s.e.m. (standard error of the mean); n = 9. Conditions: [SST] = 0.003, 0.01, 0.03, 0.05, 0.1, 0.3, 0.5, 1, 3, and 7 μM; 20 mM HEPES, pH 7.4, 150 mM NaCl. **b,** Change in the fluorescence intensity of the $GRAB_{SST}$ sensor upon addition of SST incubated with or without metal ions. Data are presented as mean ± s.e.m. (standard error of the mean); n = 20 (without metal ions), n = 10 (with metal ions). **c,** Fluorescence measurements of the $GRAB_{SST}$ sensor after administration of metal ions and vehicle (buffered solution). Data are presented as mean ± s.e.m. (standard error of the mean); n = 4–10 per group. Conditions: [SST] = 0.5 μM; [MCl_2] = 0.5 μM; 20 mM HEPES, pH 7.4, 150 mM NaCl; 24 h incubation; constant agitation. The vertical lines indicate time points when the $\Delta F/F_0$ values were quantitatively analyzed and compared between groups.

a

b

Coordinating residue(s)	Models	ΔE (kcal/mol)	$\bar{v}_{max}$ (cm^{-1})	g_z
Ala1	**Ala1-I**	10.9	13900	2.191
	Ala1-II	11.8	13200	2.184
	Ala1-III	17.2	11700	2.190
Ala1 & Lys4	**Ala1Lys4-I**	28.8	10500	2.168
	Ala1Lys4-II	33.7	11000	2.179
Ala1 & Cys14	**Ala1Cys14-I**	4.0	16800	2.165
	Ala1Cys14-II	6.5	11500	2.194
	Ala1Cys14-III	9.7	9600	2.179
	Ala1Cys14-IV	12.9	11400	2.178
Cys14	**Cys14**	5.9	13000	2.209
Lys9 & Cys14	**Lys9Cys14**	0.0	15100	2.170

c

Model Ala1Cys14-II
ΔE = 2.5 kcal/mol

Model Ala1Cys14-III
ΔE = 5.7 kcal/mol

Model Ala1Cys14-IV
ΔE = 8.9 kcal/mol

Extended Data Fig. 2 | DFT models of Cu(II)(SST). a, Energy-minimized geometry of SST. The amino acid residues that can coordinate to Cu(II) are circled. Yellow, gray, blue, red, and white balls indicate S, C, N, O, and H atoms, respectively. H atoms bonded to carbon atoms are omitted for clarity. **b**, Comparison of the DFT models of Cu(II)(SST). Total 11 models were constructed and their relative potential energies (ΔE in kcal/mol), the TDDFT-calculated Abs band energies ($\bar{v}_{max}$ in cm^{-1}), and EPR g_z parameters are summarized. The model **Ala1Cys14-I** exhibits the highest $\bar{v}_{max}$ and the smallest g_z value that reproduce the experimental results, with a reasonable stability given the DFT energy error (*ca.* 5 kcal/mol). **c**, DFT models (**Ala1Cys14-II–IV**) of Cu(II)(SST). The Cu(II) center is coordinated to the *N*-terminal primary amine (Ala1) and water molecules that are hydrogen bonded to Cys14. Three different structures obtained with variations in hydrogen bonding are given, with their relative potential energies at the bottom. The truncated Cu(II) sites used for spectroscopic calculations are depicted at the bottom. Compared to the Cu(II)-free SST structure (coloured lines), major configurational changes were observed and highlighted in dashed circles. Orange, yellow, gray, blue, red, and white balls indicate Cu, S, C, N, O, and H atoms, respectively, and H atoms bonded to carbon atoms are omitted for clarity.

Extended Data Fig. 3 | Receptor-binding studies of SST incubated with Aβ$_{40}$. a, Change in the fluorescence of the GRAB$_{SST}$ sensor upon addition of SST treated with Aβ$_{40}$ in the absence and presence of metal ions. Data are presented as mean ± s.e.m. (standard error of the mean); n = 19–21 per group. **b,** Fluorescence measurements of the GRAB$_{SST}$ sensor after administration of metal-added and metal-free Aβ$_{40}$ without SST. Data are presented as mean ± s.e.m. (standard error of the mean); n = 10 per group. Conditions: [SST] = 0.5 μM; [MCl$_2$] = 0.5 μM; [Aβ$_{40}$] = 0.5 μM; 20 mM HEPES, pH 7.4, 150 mM NaCl; 24 h incubation; constant agitation. The vertical lines indicate time points when the $\Delta F/F_0$ values were quantitatively analyzed and compared between groups.

nature research

Corresponding author(s): Mi Hee Lim, Seung-Hee Lee, Kiyoung Park

Last updated by author(s): May 8, 2022

Reporting Summary

Nature Research wishes to improve the reproducibility of the work that we publish. This form provides structure for consistency and transparency in reporting. For further information on Nature Research policies, see our Editorial Policies and the Editorial Policy Checklist.

Statistics

For all statistical analyses, confirm that the following items are present in the figure legend, table legend, main text, or Methods section.

n/a	Confirmed	
☐	☒	The exact sample size (*n*) for each experimental group/condition, given as a discrete number and unit of measurement
☐	☒	A statement on whether measurements were taken from distinct samples or whether the same sample was measured repeatedly
☐	☒	The statistical test(s) used AND whether they are one- or two-sided *Only common tests should be described solely by name; describe more complex techniques in the Methods section.*
☐	☒	A description of all covariates tested
☐	☒	A description of any assumptions or corrections, such as tests of normality and adjustment for multiple comparisons
☐	☒	A full description of the statistical parameters including central tendency (e.g. means) or other basic estimates (e.g. regression coefficient) AND variation (e.g. standard deviation) or associated estimates of uncertainty (e.g. confidence intervals)
☐	☒	For null hypothesis testing, the test statistic (e.g. *F*, *t*, *r*) with confidence intervals, effect sizes, degrees of freedom and *P* value noted *Give P values as exact values whenever suitable.*
☒	☐	For Bayesian analysis, information on the choice of priors and Markov chain Monte Carlo settings
☒	☐	For hierarchical and complex designs, identification of the appropriate level for tests and full reporting of outcomes
☐	☒	Estimates of effect sizes (e.g. Cohen's *d*, Pearson's *r*), indicating how they were calculated

Our web collection on statistics for biologists contains articles on many of the points above.

Software and code

Policy information about availability of computer code

Data collection	Agilent 6530 Accurate Mass Quadrupole Time-of-Flight (Q-TOF) mass spectrometer with an ESI source (Agilent, Santa Clara, CA, USA)
	Agilent 8453 UV–Vis spectrophotometer (Agilent, Santa Clara, CA, USA)
	ChemiDoc MP imaging system (Bio-Rad, Hercules, CA, USA)
	JASCO-815 150-L CD spectropolarimeter (for CD; Jasco Inc., Tokyo, Japan)
	SpectraMax M5 microplate reader (Molecular Devices, Sunnyvale, CA, USA)
	HORIBA QuantaMaster QM 400 spectrophotometer (HORIBA, Kyoto, Japan)
	ZEISS ApoTome2.0 (Carl ZEISS, Oberkochen, Germany)
	Zeiss LSM 880 (Carl ZEISS, Oberkochen, Germany)
	Bruker EMXplus EPR spectrometer (Bruker BioSpin, Silberstreifen, Rheinstetten, Germany) equipped with an ER 4141VT digital temperature control system (Bruker BioSpin) and an ER 4119HS cavity (Bruker BioSpin)
	JASCO J-1500 CD spectrometer (for MCD; Jasco Inc., Tokyo, Japan)
	Tecnai F20 transmission electron microscope (FEI Company, Eindhoven, Netherlands)
	Zeiss LSM 880 (Carl ZEISS; KARA)

Data analysis	OriginPro 9.0 ImageJ v1.53k IBM SPSS® W95EPR program Gaussian 09-d.01 package ORCA 4.2.0 AutoDock Vina v.1.2.0 Pymol 2.0.7 Coloc2 plugin in Fiji 2.1.1 software

For manuscripts utilizing custom algorithms or software that are central to the research but not yet described in published literature, software must be made available to editors and reviewers. We strongly encourage code deposition in a community repository (e.g. GitHub). See the Nature Research guidelines for submitting code & software for further information.

Data

Policy information about availability of data

All manuscripts must include a data availability statement. This statement should provide the following information, where applicable:

- Accession codes, unique identifiers, or web links for publicly available datasets
- A list of figures that have associated raw data
- A description of any restrictions on data availability

All experimental details and data supporting the findings of this study are available within the paper and its Supplementary Information. Source data are provided with this paper. The data are also available from the corresponding authors upon reasonable request.

Field-specific reporting

Please select the one below that is the best fit for your research. If you are not sure, read the appropriate sections before making your selection.

☒ Life sciences ☐ Behavioural & social sciences ☐ Ecological, evolutionary & environmental sciences

For a reference copy of the document with all sections, see nature.com/documents/nr-reporting-summary-flat.pdf

Life sciences study design

All studies must disclose on these points even when the disclosure is negative.

Sample size	No statistical methods were used to predetermine the sample size for in vitro experiments. The sample size chosen for each experiment was sufficient to support the conclusions. For receptor-binding studies using the GRAB sensor, the sample sizes varied between 9 and 23 to verify experimental reproducibility and to obtain mean +/- s.e.m. Sample sizes are indicated in the figure legends wherever applicable.
Data exclusions	All data sets are included and analyzed.
Replication	Three independent experiments were performed to ensure reproducibility, and all the replicas were significantly correlated.
Randomization	No formal randomization was done because this was not applicable in our study.
Blinding	No formal blinding was done because this was not applicable in our study.

Reporting for specific materials, systems and methods

We require information from authors about some types of materials, experimental systems and methods used in many studies. Here, indicate whether each material, system or method listed is relevant to your study. If you are not sure if a list item applies to your research, read the appropriate section before selecting a response.

Materials & experimental systems

n/a	Involved in the study
☐	☒ Antibodies
☐	☒ Eukaryotic cell lines
☒	☐ Palaeontology and archaeology
☒	☐ Animals and other organisms
☒	☐ Human research participants
☒	☐ Clinical data
☒	☐ Dual use research of concern

Methods

n/a	Involved in the study
☒	☐ ChIP-seq
☒	☐ Flow cytometry
☒	☐ MRI-based neuroimaging

Antibodies

Antibodies used	Anti-Aβ antibody (6E10) (catalog #: SIG-3920; Covance, Princeton, NJ, USA) Anti-SST antibody (catalog #: BML-SA1267-0025; Enzo Life Science, Ann Arbor, MI, USA) Goat anti-rabbit secondary antibody conjugated with horseradish peroxidase (catalog #: W4011; Promega, Madison, WI, USA) Goat anti-mouse secondary antibody conjugated with horseradish peroxidase (catalog #: 10004302; Cayman, Ann Arbor, MI, USA) Alexa Fluor 647-goat anti-mouse secondary antibody (catalog #: A-21235; Invitrogen, Carlsbad, CA, USA)
Validation	All commercial antibodies have been validated and published, with relevant information existing in the pertaining website. For anti-Aβ antibody (6E10), it is reactive to amino acid residue 1-16 of human beta amyloid. The epitope lies within amino acids 3-8 of beta amyloid (EFRHDS). Application: WB (Quality tested), Direct ELISA, IHC-P (Verified), IHC-F, EM, ICC (Reported in the literature, not verified in house). For anti-SST antibody, it recognizes the C-terminus of somatostatin-14 in a wide range of mammalian and non-mammalian species, including mouse and human. It does not cross-react with the N-terminus of somatostatin-28. Applications: IHC, Immunoelectron microscopy.

Eukaryotic cell lines

Policy information about cell lines

Cell line source(s)	HEK293T and SH-SY5Y cells were purchased from the American Type Culture Collection (ATCC; Manassas, VA, USA).
Authentication	Cells were authenticated by the ATCC. No further authentication of cell lines was performed by the authors.
Mycoplasma contamination	Cells were routinely tested for mycoplasma every 1 year, and the cell lines used tested negative for mycoplasma contamination.
Commonly misidentified lines (See ICLAC register)	No commonly misidentified cell lines were used.